Applied Thermal Engineering 299 (2026) 131209

Contents lists available at ScienceDirect

Applied Thermal Engineering

journal homepage: www.elsevier.com/locate/apthermeng

Research Paper

A system-level simulation framework for developing next-generation marine gas engines

Aneesh Vasudev [a,*], Jeyoung Kim [a], Kian Golbaghi [a], Martin Axelsson [b], Ben Smulter [b], Jari Hyvönen [b], Maciej Mikulski [a,*]

[a] Efficient Powertrain Solutions (EPS), School of Technology and Innovation, University of Vaasa, Wolffintie 34, FI-65200 Vaasa, Finland
[b] Engine Research and Technology Development at Wärtsilä Marine Solutions, Vaasa, Finland

ARTICLE INFO

Keywords:
RCCI
Physics-based model
Model-based optimisation
Emissions-efficiency trade-off
Marine gas engines

ABSTRACT

Reactivity-controlled compression ignition (RCCI) is a proven highly efficient and fuel-flexible combustion concept, yet its industrialisation is burdened by the multitude of operating parameters, which have strong nonlinear interactions. These characteristics challenge development of control algorithms, hindering efficient engine calibration. Existing model-based approaches struggle to resolve these nonlinearities with sufficient speed and fidelity, relying either on heuristic submodels or computationally heavy computational fluid dynamics simulations. The present study addresses this by employing an advanced performance-oriented combustion model, featuring detailed chemical kinetics, semi-predictive fuel-stratification and in-cylinder mixing grounded on the turbulence-energy cascade. Validation against a 200 mm-bore, single-cylinder research engine reveals combustion phasing predicted within ±3 °CA, and NO_X and CH_4 emissions below 35% error, representing best-in-class predictive performance. The mesoscale model is subsequently coupled with a validated 1D air-path model, enabling efficient multi-cylinder simulations with turbocharger and air-path thermal management. For the first time, this comprehensive simulation framework is applied to model-based development of a new engine, based on the Wärtsilä 20-series turbo-diesel platform. The retrofit transmutes towards gas–diesel RCCI operation, assuming minor hardware modifications. The optimal compression ratio using the stock turbocharger is identified as 14:1, yielding a peak indicated efficiency of 49.4% at 75% load. Load-range-averaged NO_X is half IMO's Tier II limit, while CH_4 emissions reach 2.9 g/kWh, except at low loads. Air-management optimisation further elevates indicated efficiency to 51.2%, with NO_X reduced to 0.16 g/kWh, below the automotive Euro VI limit. The above explorations cover 1880 simulation runs, each taking under 20 min until convergence.

1. Introduction

1.1. Background

Stringent marine transport regulations from the International Maritime Organization (IMO), such as the Tier III emissions norms issued in 2016, and the sulphur cap in Annex VI to MARPOL in 2020, are designed to cut greenhouse gas emissions [1]. Further, holistic measures introduced carbon intensity index, ship energy efficiency management plan, etc. according to IMO's MEPC77 [2]. At the same time, shipbuilders face commercial challenges like innovation and manufacturing, cost inflation, supply chain disruptions and stiff competition. Thus, novel technologies must be developed and deployed more swiftly and efficiently.

Emissions reduction from marine powerplants follow three paths: fuelling, combustion technology and exhaust aftertreatment [3]. Liquified natural gas is a popular [2] sulphur-free fuel, yielding a 25% reduction in carbon footprint [4] without needing aftertreatment scrubbers. Contemporary marine gas engines [5] employ either spark-ignited (SI) lean-burn combustion or dual-fuel pilot diesel-ignited (DF) combustion. SI technology uses pre-chamber-assisted ignition [6] to improve the lean mixture's flame propagation and combustion stability [7]. High pressure direct injection improves filling efficiency [8] and extends the operating range previously limited by knock. DF engines, on the other hand, use pilot injected diesel-like fuel to assist ignition of the main fuel, natural gas (NG). This also allows running in pure diesel mode for back-up. Generally, gas engines benefit from smokeless combustion, i.e., 97% less black carbon and 93% less particulate matter than diesel. Engine-out NO_X is about five times lower, complying with IMO Tier III. However, these engines cannot outperform the thermal efficiency of

* Corresponding authors.
E-mail addresses: aneesh.vasudev@uwasa.fi (A. Vasudev), maciej.mikulski@uwasa.fi (M. Mikulski).

https://doi.org/10.1016/j.applthermaleng.2026.131209
Received 3 February 2026; Received in revised form 8 April 2026; Accepted 25 April 2026
Available online 27 April 2026

Nomenclature

Abbreviations

BR	blend ratio
bTDC	before top dead centre
CAC	charge air cooler
CBV	charge air cooler bypass valve
CDC	conventional diesel combustion
CFD	computational fluid dynamics
CHR	cumulative heat release
CR	compression ratio
DF	dual fuel
DI	direct injection
EGR	exhaust gas recirculation
EGT	exhaust gas temperature
EVO	exhaust valve opening
HRF	high-reactivity fuel
HRR	heat release rate
IMEP	indicated mean effective pressure
IMO	International Maritime Organization
ISAC	indicated specific air consumption
ITE	indicated thermal efficiency
IVC	intake valve closing
LFO	light fuel oil
LRF	low-reactivity fuel
MZM	multizone model
NG	natural gas
NPD	new product development
PFI	port fuel injection
PR	pressure ratio
PRR	pressure rise rate
RCCI	reactivity-controlled compression ignition
SOI	start of injection
T/C	turbocharger
TIT	turbine inlet temperature
UHC	unburnt hydrocarbons
VCR	variable compression ratio
VVA	variable valve actuation

Variables

λ	air-fuel equivalence ratio
γ	ratio of specific heats
h	specific enthaply
NO_X	oxides of nitrogen
P_{iman}	intake manifold pressure
P_{max}	peak in-cylinder pressure
T_{iman}	intake manifold temperature

diesel, especially in the low- to mid-load ranges [9,10]. With the prospects of tightening regulations, this technology is challenged in surpassing the IMO Tier III barrier, coupled with low methane slip [11].

Ultra-low emissions of NO_X with simultaneous improvement in thermal efficiency are the hallmark of reactivity-controlled compression ignition (RCCI) engines. RCCI uses two fuels: a low-reactivity fuel (LRF) and a high-reactivity fuel (HRF). Combustion propagates via volumetric auto-ignition and typical peak temperatures are $\leq$1800 K. It is fuel-flexible, and demonstrators have tested various combinations of LRF (e.g., gasoline [12], alcohols – ethanol [13] or pentanol [14], gases – methane [15]) with HRF (e.g., mineral diesel [15], biodiesel [13]). Doosje et al. [15] demonstrated NO_X emissions below 0.4 g/kWh in a diesel and NG-fuelled retrofit truck engine. Hanson et al. [16] observed an indicated efficiency of 53% using gasoline and diesel, but values as high as 57% were achieved [17] by tailoring fuel reactivity with additives. The on-road sector has diminishing interest in RCCI because it is now focused on electrification, but RCCI has progressed in the marine sector. For instance, the authors' research group [18] has worked with Wärtsilä Finland Oy to advance RCCI technology to sea trials on board M/V Aurora Botnia.

RCCI's widespread adoption is hindered by its limited operating window. The specific issues are high peak pressure (P_{max}) and pressure rise rates (PRR) during high loads, and high unburnt hydrocarbon (UHC) emissions at low loads [19]. A promising method of broadening the load range is variable valve actuation (VVA) [20]. Different VVA strategies can control the apparent compression ratio, temperature at intake valve closing (IVC) and residual burnt gas amount. Direct injection of LRF is another way of improving low-load performance [21]. The myriad of potential options translates into increasing hardware complexity and a huge burden for engine controls calibration and optimisation during new product development (NPD). Atkinson [22] calculates that 10^{n+2} measurement points are required for n control parameters to resolve the large interactions and non-linearities inherent to RCCI engines [23]. The exponentially growing calibration space (n) magnifies resources for NPD, which is heavily reliant on physical prototypes. Frontloading simulations earlier in the development phase shrinks test-loops by 10–15%, reducing 'concept-to-market' time by 29% [24]. Physics-based system-level [25] models are a cornerstone of such model-based development approaches.

The limitations of experiment-based optimisation are apparent in Ansari et al.s work [26], where a mere 120 test points covered the influence of six factors, such as LRF blending fraction and air excess ratio (λ), across six load cases. The resulting linear partial factorial regression models grossly oversimplify the non-linear responses of emissions, exhaust temperature and specific fuel consumption. These were used to minimise fuel and urea consumption with the constraint of satisfying US Tier 3 EPA emissions standard. The eventual validation showed, for instance, NO_X overpredicted on an average by 90%.

High-fidelity computational fluid dynamics (CFD) is widely used for fundamental-level studies and detailed component design, such as spray formation and combustion propagation in the work of Ao et al. [27]. They used a closed-cycle CFD model to investigate the influence of pilot injection pressure and gas injection pressure on methane slip, combustion characteristics and emissions. This was later combined with hydrogen blending in a multi-strategy coupling approach. The optimisation was performed informally based on parametric sweeps and scenario-based comparisons. Thus, CFD models are unsuitable for system-level optimisation. For instance, Jeong et al. [28] mentioned that one full-cycle combustion simulation required 165 h (1 week) on an Intel™ Xeon W-2265 workstation. Thus, their utility is restricted by the number of factors and limited to surrogate-based optimisation.

Empirical and semi-empirical combustion models currently form the mainframe of full engine system simulations. Cong et al. [29] developed a simplified Wiebe heat release model coupled with basic submodels to simulate a dual-fuel marine engine. Based on 112 results generated from this simple model, they proposed a second-order polynomial regression to model engine outputs according to the input parameters, including intake pressure, temperature and blend ratio. They employed an optimisation approach, based on multi-objective particle swarm optimisation, to fine-tune engine fuel consumption and NO_X emissions. Park et al. [30] studied a dual-fuel CI engine using a two-zone multi-component Wiebe function in GT-Suite. Validating against the diesel mode, they employed Latin hypercube sampling and a multi-objective Pareto optimisation approach to identify the most effective parameters for dual-fuel engine performance and emissions. Such approaches are computationally economical but suffer from the requirement of a large training

dataset from either experiments or higher fidelity simulations [31], thus restricting predictivity.

In the context of reactivity-based combustion, chemical-kinetics multizone models (MZM) occupy a middle ground, with predictivity similar to CFD (including emissions) and simulation time in the order of minutes. For example, in optimising the operating parameters of an NG-diesel RCCI marine engine, Mikulski et al. [32] employed both MZM and a 1D model of the air-path, running them in a decoupled manner. The first optimisation ran solely on the MZM, followed by the air-path simulation, with imposed burn rate from the previous run. They considered five factors (T_{IVC}, λ_{diesel}, NG blend fraction, SOI_{diesel} and EGR) across four load points. Surrogate-type optimisation revealed an indicated efficiency of 47.8% at 75% loading on stock engine hardware, with CO and UHC emissions well below legislation limits. Furthermore, optimising the compression ratio to 15.2:1 improved indicated efficiency to 51.8%.

In summary, current state-of-the-art in system-level models of RCCI engines for use especially in large-scale DoE studies and optimisation fall short along the following lines: (i) either data-driven thus requiring large datasets, while predictivity being limited to the boundaries of the training data; or (ii) despite being physics-based, too computationally heavy to practically explore large design space (five factors or more); or (iii) not comprehensive in incorporating chemical kinetics-based combustion and emissions predictions with multi-cylinder simulation including turbocharger; or (iv) demonstrations that have not been parameterised and validated to the scale of marine engines. Thus, the authors of the present work have contributed to closing this methodological gap through the interconnected Clean Propulsion Technologies [33] and CASEMATE [34] projects. Recent advances within this ecosystem by Modabberian et al. [31] demonstrated that, with governing assumptions tailored to marine combustion systems, the University of Vaasa Advanced Thermo-kinetic Zonal Model (UVATZ) can, after only minimal calibration, generate a representative multidimensional dataset suitable for developing control strategies for the next generation of marine RCCI combustors. In follow-up work, Kakoee et al. [35] developed a complementary one-dimensional framework by dynamically coupling UVATZ with the engine air-path model, using reference data from a Wartsila 31 single-cylinder research engine. This framework has since been successfully applied, among others, to demonstrate proof-of-concept of electro-hydraulic valve actuation (EHVA)–enabled load extension in RCCI [36] and to design new calibration for hydrogen-enriched RCCI operation [37].

The present study extends the UVATZ mesoscale modelling ecosystem, described above, towards full multi-cylinder engine optimisation framework. The goal is bridging fundamental developments in computational methods (Objective 1) with demonstration of predictive capability in a relevant marine application (Objective 2). The study's objectives are:

Objective 1: Develop a rapid-prototyping framework for predictive RCCI simulations of turbocharged multi-cylinder engines. The framework must provide modularisation of the cylinder-individual UVATZ solution for performance, combustion phasing and detailed emissions as functions of all RCCI control parameters. The fully predictive co-simulation should maintain computational efficiency (~20 min per load case) suitable for turbocharger matching and engine-level optimisation studies.

Objective 2: Demonstrate the modelling framework's impact by integrating it into a model-based engine-development workflow. A representative and industrially relevant use case is selected, i.e., retrofitting a Wärtsilä 4L20 diesel platform for ultra-efficient RCCI operation. Single-cylinder RCCI experiments and multi-cylinder diesel engine tests are used to train the combustion and air-path submodels. The validated framework is then applied to perform advanced model-based optimisation to identify hardware modifications that maximize engine performance under constraints arising from emissions, component durability and turbocharger sizing. Control degrees of freedom include fuel-blend ratio, injection timing and active thermal-management strategies.

2. Methodology

The framework for predictive RCCI engine simulations constitutes a 1D gas dynamics model and a multizone combustion model. The former is used to model the fuel-path and air-path, including turbocharger (T/C) dynamics. It is built in the commercial software GT-Power™. The combustion model, hereafter referred to as UVATZ (University of Vaasa Advanced Thermo-kinetic multi-Zone model), is physics-based, chemical-kinetics oriented, therefore capable of capturing both heat release and emission formation. Both models are coupled as co-simulation with the GT-Power solver acting as the master. Although the toolchain encompasses exhaust aftertreatment devices [35], they are excluded from the present work. Details of both models and the coupling methodology are discussed in Section 2.2.

Parameterisation of the modelling framework follows a Wärtsilä 200 mm-bore, mid-speed platform [38]. UVATZ was developed separately and validated [39] on a single-cylinder NG-diesel RCCI research variant of the engine. This engine will be referred to as 'Engine A' going forward. The 1D model, on the other hand, was developed and validated [40] on the present study object, a four-cylinder turbo-diesel version of the 200 mm bore platform, which hereafter will be referred to as 'Engine B'. Section 2.1 describes both engines' test rigs.

The principle of separate submodel validation aligns with typical powertrain development workflow, which starts from combustion concept characterisation on single-cylinder research engine, through to integration on the production platform, including component tailoring. The research objective is to virtually retrofit the stock Engine B to operate on NG-diesel RCCI, so Section 2.3 describes the development of such a prototype through the model. The emphasis is on dissecting RCCI's multi-criteria optimisation problem into manageable, smaller optimisation campaigns.

2.1. Research object

2.1.1. Engine A

The prototype single-cylinder research engine (SCRE) is based on the Wärtsilä 20 dual-fuel, mid-speed platform [38]. Compared to the commercial variant, its heavy modifications include a variable compression ratio (VCR) and VVA for extended calibration flexibility. Table 1 lists the engine specifications for the RCCI experiments. The fuel system incorporates single-needle injectors for direct high-reactivity pilot fuel injection and a multi-point gas injection system upstream of the intake valves. ISO 8217-compliant light fuel oil (LFO) is the pilot fuel; natural gas with a methane number of 80 is the main fuel. Fuel- and air-path control is via a Speedgoat/CANape Rapid prototyping platform using in-house developed Simulink codes.

The SCRE is equipped with a charge air system with two compressors, a charge air dryer and a charge air temperature conditioning unit. A buffer tank on the intake side is dimensioned to replicate the pulsations observed in multi-cylinder engine manifolds. A buffer tank and a backpressure valve on the exhaust side mimic the pulsations and turbine operation.

Data acquisition for this study includes high frequency measurements of in-cylinder pressure recorded over 300 consecutive cycles with a resolution of 0.2 ^{0}CA. Consequently, the engine's performance is quantified by further processing the data to calculate apparent heat release (*HRR*), crank angle for X% fuel energy released (CAX) and performance indicators such as indicated mean effective pressure (*IMEP*). Appendix A describes the postprocessing routine. The measurement

Table 1
Technical specification of the engines used to identify the modelling framework.

	Engine A (Wärtsila SCE)	Engine B (Wärtsila 4L20 diesel)
Scope	RCCI combustion validation	Multi-cylinder engine optimisation
Cylinder configuration	Single-cylinder research engine (four-stroke)	Four-cylinder, in-line (four-stroke)
Nominal speed	1000 rpm	
Stroke / Bore	1.4	
Swept volume	8.8 L /cylinder	
Compression ratio	variable	16:1
Charing system	External compressor with air temperature and pressure control (up to 10 bar)	Twin-entry single-stage turbocharger up to 5 bar
HRF system	ISO 8217 LFO; high pressure common-rail; solenoid injector	ISO 8217 LFO; high-pressure common-rail; nine-hole solenoid injector
LRF system	Natural gas (MN = 80), low pressure PFI 20 bar	–
Valve train	Fully flexible EHVA four valves/cylinder	Cam-based four valves/cylinder (variable exhaust valves)
Engine control system	Speedgoat / CanApe Rapid control prototyping platform	

system also involves temperature and (fast) pressure measurement in intake and exhaust ports. Low-frequency measurement data monitor liquid fuel consumption, using gravimetric balance and gas (air and NG) mass flow rates using Coriolis flow meters. Telemetric thermocouples installed in cylinder head, piston and liner provide temperatures of cylinder components.

2.1.2. Engine B

Wärtsilä's four-cylinder turbo-diesel engine, the W4L20 [41] is the basis for RCCI adaption. Its bore and swept volume are identical to the single-cylinder counterpart, but the engine is equipped with a mechanical camshaft-based valvetrain with limited ability to shift exhaust valve timing (Miller cycle). The multi-cylinder engine is coupled with a single-stage twin-scroll turbocharger, enabling intake pressures of up to 5 bar. The pressurised intake air is cooled via a water-cooled charge-air cooler. The total air mass flow rate is measured via a venturi-based flow meter [42].

Liquid fuel (LFO) is delivered via centrally mounted, nine-hole solenoid injectors from an ultra-high pressure common-rail injection system. Fuel consumption is measured gravimetrically. Injection parameters and other engine control variables are managed via Speedgoat rapid control prototyping platform. The engine is coupled to a squirrel-cage induction motor acting as a generator to impose load. The engine's rated maximum power is 0.8 MW. Engine speed is maintained at a constant 1000 rpm, and the generator is managed via an ABB programmable logic controller.

In-cylinder pressure for air-path model calibration is measured using a piezoelectric pressure transducer (Kistler 6125C) with a piezoresistive amplifier at all cylinders. High-frequency pressure signals and crankshaft position are recorded via an optical encoder (Kistler 2614CK) with 0.1 ^{0}CA resolution. The HBM T10FM torque transducer measures engine brake torque. Multiple temperature and pressure sensors are installed throughout the intake and exhaust lines, as well as in the cooling and lubrication circuits (Fig. 1) for comprehensive model validation. Coolant and oil temperatures are regulated by the engine's built-in thermostats, with minor variations of engine load and speed. These variations remained insignificant from the modelling perspective, as the wall temperatures are directly imposed. The 4L20 does not have thermally characterised cylinders, so the temperature change with operating conditions are assumed the same as in the diesel test run of the single-cylinder version.

All thermal parameters and low-frequency signals (sampled at 1 Hz)

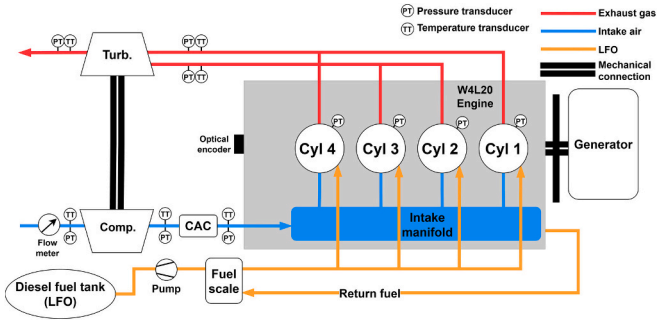

Fig. 1. Schematic of the multi-cylinder research engine platform (Engine B) with instrumentation relevant for air-path model validation.

are managed by an in-house automation system. High- and low-frequency data are collected by a commercial data acquisition system (Dewesoft® Sirius). Dewesoft®X, which includes an integrated combustion engine analysis module, is used for real-time signal processing. This includes filtering of the pressure signals, in-cylinder pressure pegging (referenced to intake manifold pressure at intake bottom dead centre) and real-time combustion analysis (*IMEP*, *HRR*, etc.) based on the first law of thermodynamics with a single-zone model.

2.2. Modelling framework

2.2.1. RCCI combustion model

UVATZ is a custom combustion model built specifically for low-temperature combustion concepts like RCCI. It is coded in C++ and simulates the closed part of the four-stroke cycle. The governing assumption is that in-cylinder fluid flow is axisymmetric, based on which combustion chamber volume is discretized coarsely into a series of coaxial zones (Fig. 2). The zonal arrangement, including their individual volumes, has been calibrated [39] in order to phenomenologically capture DI pilot fuel stratification. The number of zones is set to 12, balancing computation demand with accuracy [43]. Each zone is a homogeneous reactor, while the ensuing network of reactors are setup such that all share a common pressure. This assumption is based on the condition that the zones' pressures equilibrate at the speed of sound, a rate much faster than advection. Consequently, a zone's volume relative to another changes, resulting in interzonal work transfer. Thus, the need to solve momentum balance is withdrawn. However, heat and mass flow between zones are modelled phenomenologically with a 0-dimensional energy-cascade turbulence sub-model [44].

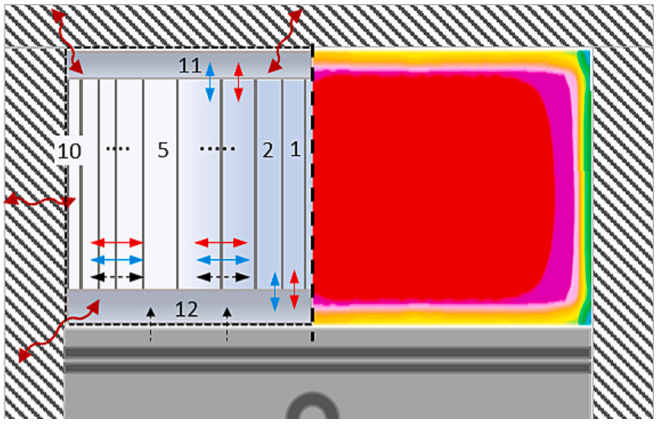

Fig. 2. Schematic of zonal arrangement in UVATZ model. Red arrows indicate heat flow, blue arrows indicate mass flow and black arrows indicate work transfer. (For interpretation of the references to colour in this figure legend, the reader is referred to the web version of this article.)

The decoupled nature of the injection event from combustion in RCCI eliminates the need to track the spray formation rigorously. Thus, the focus of fuel injection modelling is shifted to the ensuing bulk in-cylinder stratification, critical to RCCI combustion control. Accordingly, the adopted approach predicts the radial stratification of HRF near start of combustion, via a CFD derived correlation on main engine operating parameters. Appendix A shows the equations, while the derivation is seen in an earlier work [39].

Heat exchange with the environment is driven primarily by convection and follows the correlation for heat transfer coefficient by Chang et al. [45]. This is applied to the bounding zones, #10 to #12 (Fig. 2), which ultimately sets up thermal stratification across the zones. The chemical kinetics scheme by Yao et al. [46], with the extension of a skeletal oxides of nitrogen (NO_X) mechanism [47], is used. Being an in-house model, UVATZ is coded in C++ employing the libraries of Cantera [48]. Table 2 summarises the modelling choices, with complete details found in the earlier work [39]. Appendix B provides an overview of the governing equations and submodels. Note that UVATZ has been used successfully to support explorative research on RCCI, and its validity has been confirmed on several earlier campaigns, considering different marine engine platforms [39,43,49].

2.2.2. Air-path model

2.2.2.1. Baseline configuration. The baseline 1D model of air-path is parameterised to the turbo-diesel engine (Engine B in Table 1). Built in GT-Power, the piping is represented by 1D flow elements, such that every bend, connection, contraction and flow split are distinctly represented. To this end, engineering drawings of the pipework are used as much as possible, apart from direct measurements. Influence of heat transfer during pipe flow is accounted for by computing the wall temperature and employing the Colburn correlation.

A semi-predictive model for the charge-air-cooler (CAC) is used, where output temperature is correlated with individual load condition. The turbocharger model is map-based, utilising the manufacturer's performance maps for compressor and turbine. The discharge coefficient at engine cylinder ports is calibrated from flow test bench measurements, in both forward and reverse directions. The exhaust path is calibrated to capture the back pressure on the turbine and pipe wall temperatures before and after the turbine. Further details are available in the source work by Hautala et al. [40]. Finally, the 1D model uses its own solver, the explicit Runge-Kutta. The solution is cycle-to-cycle connected, with a relative tolerance of 5e-4 based on the quantities of *IMEP* and P_{max} for the combustion simulation, and average pressure and flow rate for the flow circuit.

2.2.2.2. Modifications to accommodate RCCI combustion. The model reflects the modifications made to the turbo-diesel platform for it to operate in RCCI regime. First, gas injectors are required to administer NG, with a port fuel injection (PFI) system operating at 5 bar pressure with delivery rate fixed at 20 g/s [38]. Injection duration is an operating parameter dictating the quantity of fuel. The injector model is correspondingly parameterised and connected at the intake runner of each cylinder. Second, RCCI cannot be achieved over the entire operating range with the stock compression ratio. The appropriate ratio will be determined in the optimisation, by including it as a design variable. It is assumed that the connecting rod length remains unchanged, reflecting that compression ratio is altered via piston design.

Third, intake air temperature control is necessary for regulating mixture reactivity beyond the limits admissible by fuel mixture control (*BR*) alone. Active temperature control has been shown to improve the operating window of RCCI-like concepts [51]. Note that VVA is an effective solution for even faster (cycle-to-cycle) temperature control [20]. However, VVA is not presently considered as it would compound the already large calibration space, amid uncertainties like parasitic losses in such systems [52]. While many studies realize air temperature control via external preheater, a more practical solution is installing a bypass valve before the charge air cooler. Hot air is bled from the compressor directly to the intake manifold. This is energy-efficient and realizable in multi-cylinder turbocharged applications. The by-pass

Table 2
Governing assumptions of UVATZ model.

	UVATZ features	Advantages over earlier approaches
Platform		
	▪In-house source code (C++ 14)	▪Flexible flow & reactor objects
	▪Cantera [48] thermo-kinetics library	▪>50× speedup compared to earlier [43]
	▪Robust solver CVODE [50]	▪Sim. time < 3 min per closed part 4-stroke cycle (8th gen Core® i5 workstation)
Species & Temperature stratification		
	▪12 zones (10 cylindrical +2 disk -shaped)	▪Improved stratification, fewer zones
	▪Spatially-associated fuel distribution, heat loss & emissions formation	▪Heat release (CA10, CA50, CA90) < 3 °CA error
	▪Interzonal mixing: Temperature & concentration gradient-based + Turbulence enhanced	▪Physics-based interzonal mixing
Sub-models		
	▪Wall heat loss: Chang et al. [45] correlation	▪Low temperature combustion heat loss
	▪Wall temperature: correlated to loading. Possible coupling w/ wall thermal solver	▪For piston, head & liner
	▪Chemistry mech.: Yao et al. [46] + NO scheme [47]	▪Emissions (NO_X & UCH) accuracy <30%
	▪Turbulence energy cascade (K-k-ε) model [44]	▪Physics-based turbulence model
	▪HRF stratification: Emperical model trained by CFD spray simulations [39]	▪Autonomous & emperical fuel stratification model (Factors: SOI, BR, λ)
	▪Gas exchange	▪Accurate estiamtion of charge composition and temperature
Validation	W31DF SCE RCCI [43,49] & W6L20CRDF RCCI [39]	3–10* data points from full metal engine for global calibration * assuming 5 engine control parameters

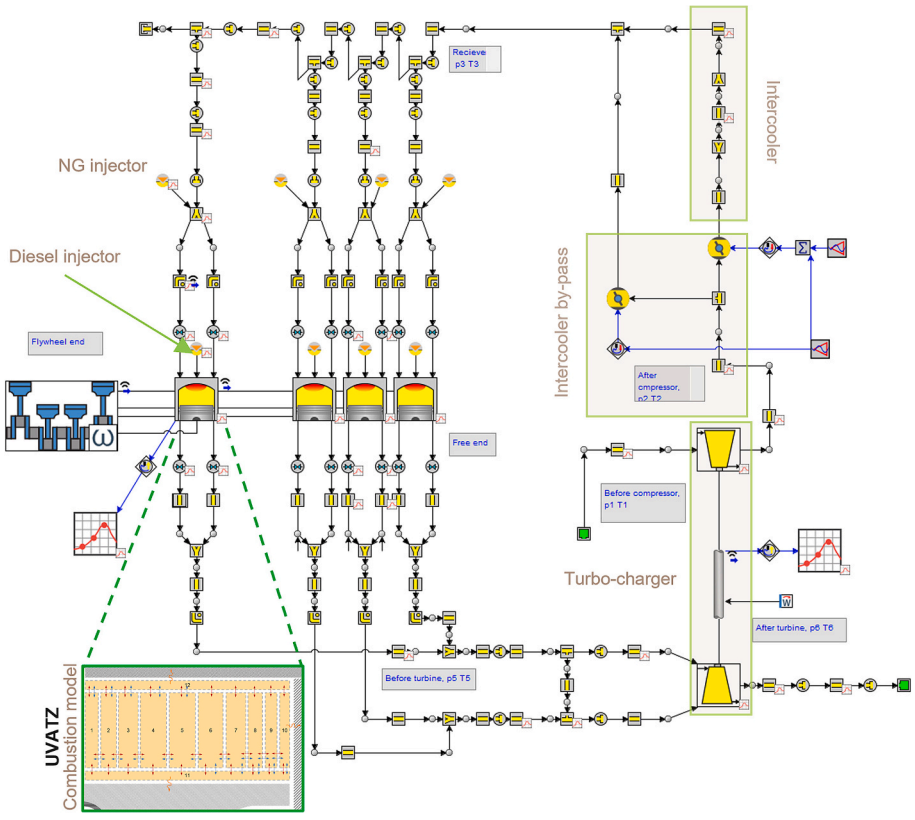

Fig. 3. Diagram of the modelling framework in GT-Power, illustrating the modifications to the air-path and fuel system on the stock 4L20 engine.

Table 3
Load cases from Engine A for validation of UVATZ.*

Case	Load [%]	λ [−]	SOI_{HRF} [°CA bTDC]	T_{iman} [K]	P_{iman} [bar]	BR [pp]	T_{wall} [K]
V1	21	ref+0.54	ref+36	ref+35.4	ref+0.31	ref-6.85	Liner: 400 Piston: 415 Head: 455
V2	50	ref+0.63	ref+31	ref+14.8	ref+1.92	ref+0.63	Liner: 420 Piston: 435 Head: 475
V3	75	ref+0.51	ref	ref+28	ref+7.1	ref*	Liner: 435 Piston: 455 Head: 490

* *ref* is the 25% load point condition from a commercial, conventional dual-fuel version [38] of the 200 mm-bore platform

valve opening is an operating parameter in the model, and measured as a percentage.

Finally, it is assumed that the same direct injector, specifically its nozzle geometry, as in Engine A is used for the retrofit Engine B. This simplifies model setup of the diesel stratification submodel, since it is calibrated (based on CFD spray simulations) to the 200 mm-bore cylinder geometry (Table 2). Fig. 3 illustrates the retrofitting on the model of the stock 4L20 engine.

Table 4
Load cases from Engine B for validation of 1D model.

Case	Load [%]	TFE [kJ]	IVO [°CA]	IVC [°CA]	EVO [°CA]	EVC [°CA]
A	25	18.29	334	507	139	386
B	50	30.07				
C	75	43.34				
D	100	57.15				

2.2.3. Coupling

The above models are coupled together to lay out the basic framework for RCCI engine simulations. The methodology is similar to that of a co-simulation approach in a functional mock-up interface [53], although not in a strict sense. UVATZ is packaged as an executable, with the air-path model (in GT-Power) as the master. Therefore, the air-path model creates an input file for UVATZ at the time of IVC, based on which the combustion sub-model is simulated for the closed cycle. The generated results file is read back into GT-Power. The input file contains data regarding the initial (IVC) thermodynamic state, gas composition, turbulent kinetic energy and length scale, geometric parameters of the combustion chamber and solver settings. The results file contains the burn rate and the burned gas composition. Based on this, the in-cylinder pressure and temperature are reconstructed in GT-Power, including the heat release rate, providing a scalable method for multi-cylinder modelling. To ensure accurate calculation of the residual mass, the species mass fraction at the last crank angle of the closed cycle is stored for use in determining the initial condition of the next cycle. This methodology is based upon our earlier work [49].

Table 5
Study campaigns to progressively optimise the operating parameters for RCCI mode on the retrofit Engine B.

Case study#	Objective	Constraints	Factors	Load Cases			
				A	B	C	D
1	max ITE_{net}	P_{max} < 225 bar	CR [–]	12.5–15.5	"	"	"
	min NO_X	TIT <850 K	SOI [^{0}CA]	58–72	"	"	"
		T/C: stock	BR [%]	73–97	"	"	"
			CBV [%]	5–45	"	"	"
2	max ITE_{net}	P_{max} < 225 bar	SOI [^{0}CA]	58–72	"	"	"
		TIT <850 K	BR [%]	73–97	"	"	"
		NO_X < 2.5 g/kWh	CBV [%]	5–45	"	"	"
		CR: fixed					
		T/C: stock					
3	max ITE_{net}	P_{max} < 225 bar	CR [–]	–	–	12.5–15.5	–
		NO_X < 2.5 g/kWh	BR [%]			85–97	
			SOI [^{0}CA]			58–72	
			P_{iman} [bar]			4.5–6	
			T_{iman} [K]			320–400	

Measures are taken to improve simulation speed and reduce the number of cycles required for convergence. First, in order to accelerate multi-cylinder simulations, only one of the four cylinders (cylinder #1) executes UVATZ for combustion results. The same burn rate and gas composition is then applied to the other cylinders to construct their pressure and temperature traces based on their individual IVC state. This saves computation resources.

Second, steady-state simulations with T/C typically require more iteration for convergence than for naturally aspirated engine models, due to the feedback loop between the exhaust and intake manifold states and rotational inertia of the T/C shaft. Therefore, the present simulation is initialised with a generic burn rate profile to ensure that intake and exhaust manifold conditions are stabilised. This is done for 40 iterations after which UVATZ is executed for 25 more iterations. Importantly, UVATZ is not executed on every cycle, instead run in a manner similar to skip-cycle sequence. The skipped cycle simply runs with the burn rate and gas composition from the prior cycle. Ultimately, these measures reduce overall simulation time to 30–40 min per case on an Intel® 8th gen. Core™ i5 workstation.

2.3. Scope of research

2.3.1. Validation of modelling framework

The combustion model (UVATZ) and the 1D air-path model were separately calibrated in earlier studies by Vasudev et al. [39] and Hautala et al. [40], respectively. Nevertheless, a validation check is performed to ensure the model's accuracy is maintained through the software version and functional updates necessary to achieve the present study's objectives. Appendix A describes the postprocessing of experimental and simulation data into relevant performance indicators.

Table 3 shows the RCCI steady-state operating points from the single-cylinder Engine A, used to validate UVATZ. The combusting cases are characterised by air-fuel equivalence ratio λ; injection timing of HRF (SOI_{HRF}); and intake manifold temperature and pressure, T_{iman} and P_{iman} respectively. *BR* refers to blend rate, indicating the amount of LRF in the total fuel mixture on an energy basis. T_{wall} is the cylinder surface temperature. The data are presented with respect to *ref*, which is a reference 25% load calibration on a conventional dual-fuel (NG-diesel) production variant of the same 200 mm-bore platform.

For combustion validation only, UVATZ is run over the four-stroke cycle as standalone whereby the gas-exchange phase is captured by a simple plenum submodel. The intake and exhaust manifold states are set as boundary conditions for two separate plenum objects. The flow through the valve is isentropic orifice flow where the effective flow area changes dynamically in accordance with the valve lift. This setup ensures that the correct initial conditions at the time of intake value closure are captured.

Table 4 shows the load cases for validation of the 1D model from the turbo-diesel engine B. The relevant input for the air-path simulation is the load demand, while the rest of the operating parameters are adjusted according to ECU calibration. Engine speed is fixed at 1000 rpm, and valve timings are fixed as shown. Combustion is not explicitly modelled; instead the burn-rate postprocessed from experimental pressure trace (via three-pressure method) is directly imposed. This approach helps set the right dynamic boundary condition in the model for the turbocharger. The sensor data relevant for validation are mention ned in Section 2.1.2.

2.3.2. Model-based optimisation

For the second research objective, the modelling framework is applied to optimise performance of a retrofit diesel engine (Engine B) operating in NG-diesel RCCI mode. The goal is to determine the engine calibration giving optimal performance. The factors considered are the *BR* for fuel blending, charge-air-cooler bypass valve position (*CBV*) for active temperature control and *SOI* for injection timing of diesel. Critically, the stock compression ratio (*CR*) inhibits extraction of RCCI's full potential because RCCI's PRR is higher than a conventional diesel, thus

demanding a lower *CR*. A consequence of modifying *CR*, in addition to RCCI's inclination to operate at leaner conditions ($\lambda > 2$), necessitates appropriate matching of the T/C. The investigation is split into three study campaigns to cover the aforementioned factors, together with constraints on durability and emissions limits. Table 5 lists the three campaigns. The baseline conditions of all the load cases follow those of Engine B from Table 4.

The first campaign's focus is to determine the system boundaries for RCCI operation. Thus, the factors, including *CR*, are independently optimised for each load point. The objective is to maximize ITE_{net}, while simultaneously minimising NO_X emissions. NO_X minimisation is included as it is uncertain at this stage whether IMO Tier III NO_X limits can be met with the stock T/C. Thus, a conservative range of 73%–97% is set for *BR*. *CR* is limited between 12.5:1–15.5:1, with the upper limit to prevent excessively harsh combustion at high loads (relates to P_{max} limit), while the lower limit ensures sufficient combustion efficiency at low loads. SOI ranges between 58^0CA and 72^0CA bTDC, corresponding to the domain of the training dataset of the HRF stratification submodel [39]. From prior experience [20], CVB below 5% results in misfire, while above 45% causes excessive NO_X, even at low loads. Finally, the optimisation constraints include P_{max} of 225 bar and turbine inlet temperature (TIT) of 850 K from the manufacturer's specifications.

The second campaign attempts to determine a geometric *CR* of the RCCI retrofit and investigates the performance that can be extracted. This is critical since the stock *CR* of 16:1 is too high for RCCI, as mentioned earlier. Also, VCR is excluded on the basis of reliability and cost. Headway is made already in study #1 in determining *CR*, which is load point specific. A global *CR* can thus be calculated by averaging, wherein load-based weights from IMO NO_X technical code [54] are adopted. The optimal performance is then determined by maximising ITE_{net} as the single objective. The factors include SOI, *BR* and *CBV*, ranging within the same limits as in study #1. The constraints include $NO_X < 2.5$ g/kWh (IMO Tier III) in addition to those from study #1.

With the stock, single-stage T/C considered thus far, the final campaign moves towards the matching of a new T/C to the RCCI engine. This is significant because commercial DF and gas engines use two-stage T/C to overcome the filling efficiency and lean mixture condition requirement ($\lambda > 2$) [55]. The goal is to estimate the targets for the T/C, such as indicated specific air consumption (ISAC) and pressure ratio, that yield better performance than observed in studies #1 and #2.

To this end, the T/C submodel is removed from the simulation, and the manifold conditions are instead directly optimised. These include intake manifold pressure (P_{iman}) and temperature (T_{iman}), as shown in Table 5. The pressure drop across the engine is fixed (a common modelling technique [20]) at 1 bar and exhaust manifold temperature is fixed at 850 K. Owing to the larger design space (five factors), the approach is demonstrated only on the 75% load point for brevity. The optimisation is performed with P_{iman} swept in discrete steps of 0.5 bar from 4.5 bar to 6 bar, selected as a feasible boost pressure range for RCCI mid-speed engines at high loading [38,39]. At each step of P_{iman}, the GT-Power's optimiser is run with the remaining factors *CR*, *BR*, SOI and T_{iman}. The objective is maximising ITE_{net} while constraining P_{max} and NO_X.

All studies use GT-Power's proprietary global optimiser based on a genetic algorithm. The stopping criterion is the total design iterations listed in Table 6, along with other optimisation settings.

Table 6
Optimiser settings.

Study#	No. of Factors	Population Size	Mutation rate	Total iterations
1	4	16	1/4	150
2	3	10	1/3	120
3	5	20	1/5	200

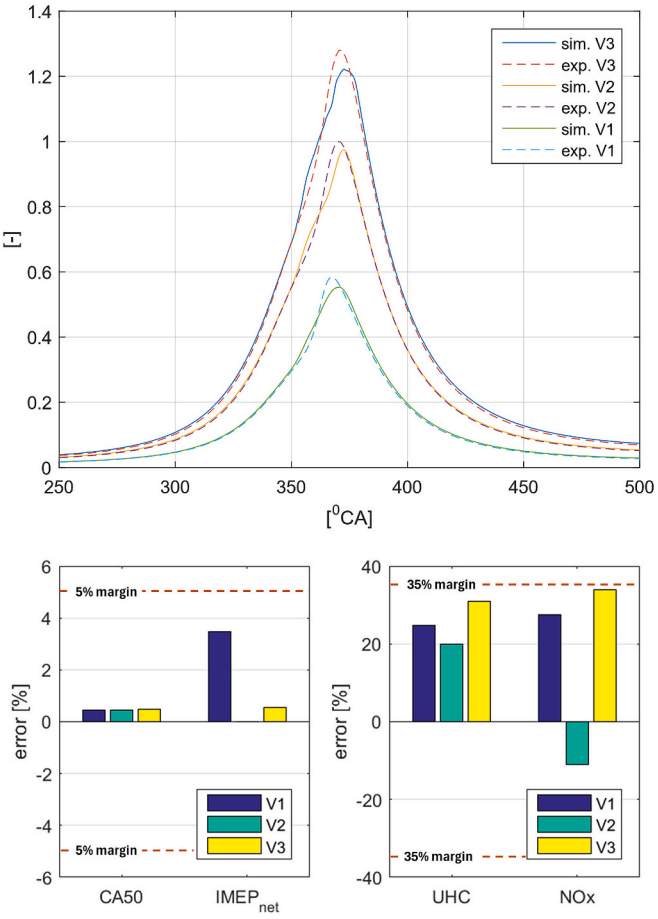

Fig. 4. Validation of UVATZ combustion model against data (Table 2) from Engine A. The pressure trace is depicted by in-cylinder pressure trace (top) and error bars (bottom) of engine performance and emissions.

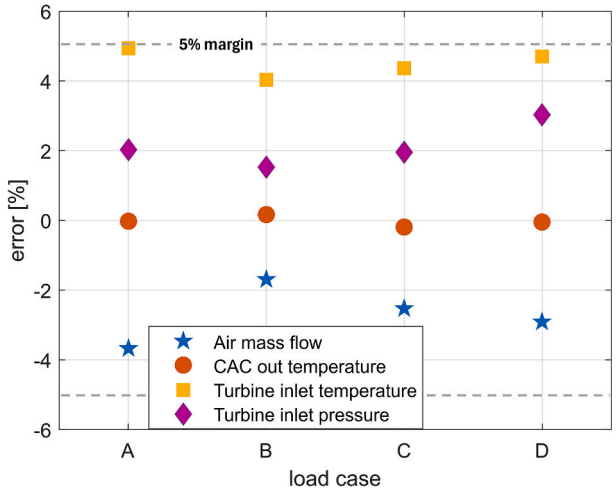

Fig. 5. Validation results of air-path model against data from Engine B, depicted by air mass flow, CAC outlet temperature, and pressure and temperature before turbine.

3. Results

3.1. Validation of modelling framework

Fig. 4 shows the validation of the UVATZ RCCI combustion model,

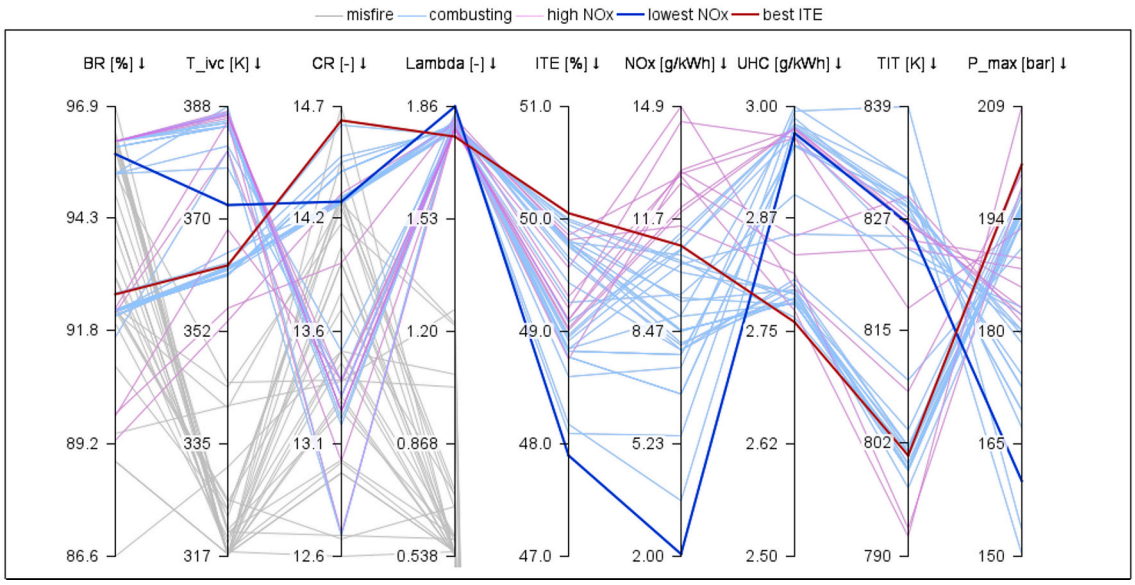

Fig. 6. The factors (BR, T_{IVC}, CR, λ) along with selected responses (ITE, TIT, P_{max}, NO_X and UHC emissions) show the optimiser design iterations for 75% load point. Combusting designs with $NO_X < 11.5$ g/kWh are shown in blue; pink indicates high-NO_X designs. For illustration, only factors of misfire designs (grey) are shown while their corresponding responses excluded. Also highlighted are the optima of best ITE and lowest NO_X. (For interpretation of the references to colour in this figure legend, the reader is referred to the web version of this article.)

with pressure trace overlaid with the measured signal in the top plot. The root mean square error is 0.41 bar, with average P_{max} error of 2.9% and occurrence of P_{max} under 1% error. The core performance indicators of interest, net IMEP and CA50, (bottom left plot) are predicted well within the 5% error margin. NO_X and UHC emissions are predicted within an error margin of 35%. Considering RCCI's ultra-low emission levels, this is state of the art [39] for such control-oriented models.

The 1D model validation was performed over four load points (Table 4) from the four-cylinder diesel engine under firing condition. The present discussion focuses solely on the air and exhaust paths of the engine. Readers interested in the diesel combustion model's results are directed to the source [40] of the research.

Fig. 5 illustrates the validation results, including the parameters air mass flow rate, intake temperature, turbine inlet pressure and turbine inlet temperature. These parameters are chosen to characterise T/C's performance and establish the boundary conditions for the in-cylinder combustion model. The air mass flow rate has around 3.7% error, while intake temperature after CAC shows good match, within 1 K over all load points. Turbine inlet pressure shows around 3% average error, while turbine inlet temperature is just within the 5% error margin at most. This level of model accuracy ensures reliable estimation of intake charge conditions, essential for RCCI combustion modelling.

3.2. System boundary for RCCI with stock turbocharger

3.2.1. Design space topology

Case study #1 considers the factors of *BR*, SOI, *CBV* position and *CR* as the design variables for optimisation of each load point about the baseline conditions in Table 4 (Engine B). Note that from here forward, variations in λ are only a result of air flow from the T/C, since the fuel energy is fixed to baseline. The dual objectives are maximising *ITE* and minimising NO_X emissions. For illustration, Fig. 6 shows the relationship between the responses and factors only for the 75% load point. T_{IVC} is shown instead of *CBV* position, along with *BR* and *CR* as the most influential factors, while the remaining parameters in the plot are responses. The misfire designs are shown in grey. Other colours represent the combusting cases. Designs producing $NO_X > 11.5$ g/kWh (IMO Tier I) are shown in pink; designs with $NO_X < 11.5$ g/kWh are in light blue. Response values for misfire cases are excluded in the figure (by restricting the axes limits) to improve plot readability.

Among the stable combusting cases, *ITE* between 48% and 50% can be achieved. Correspondingly, UHC varies between 2.75 g/kWh and 3 g/kWh. NO_X emission varies from 2 g/kWh (below IMO Tier III) to above 11.5 g/kWh (IMO Tier I). T_{IVC} ranges from 352 K to 388 K, while λ ranges from 1.75 to 1.82, still quite rich compared to marine gas engines. Hence, it is observed that high T_{IVC} and low λ leads to the high NO_X emissions. Conversely, designs with T_{IVC} too cool and high *BR* values result in misfire, indicating low mixture reactivity. The misfire boundary is 352 K and 88% for T_{IVC} and *BR*, respectively. All design iterations comply with the *TIT* and P_{max} limits constraints.

Fig. 6 highlights the 'lowest NO_X' (blue) and 'best *ITE*' (red) designs, illustrating the trade-offs between the opposing objectives. The best *ITE* of 50.05% is achieved at a high *CR* of 14.59:1, with the *BR* of 92.57% and T_{IVC} of 362.8 K. The NO_X for this design is 10.9 g/kWh, just within IMO's Tier 1 limit. The design with the lowest NO_X of 2.03 g/kWh is achieved due to λ being highest at 1.82. This is reinforced by a high *BR* value of 95.8%, and a lower *CR* of 14.2:1, despite T_{IVC} being higher, at 372 K.

In order to quantify the influence of the factors on the system's behaviour, the design iterations data is further processed using a simple, regression-based sensitivity approach. The coefficients of a linear model are fit to each response, thus determining the main effects. Table 7 shows the coefficients normalised both with respect to the factors and responses. Although not shown, the *p*-value of the responses against the factors *BR*, *CR* and T_{IVC} are on average 10^{-3}, 10^{-7} and 5×10^{-4} respectively. The relationship between the responses and SOI is not statically relevant, where p-value is around 0.5. Furthermore, the interaction effects were found to be not statically significant, therefore

Table 7
Normalised sensitivity coefficients of the main effects of the factors (rows) on the responses (columns).

	ITE	NO_X	λ	P_{max}
BR	−0.88413	−2.4968	2.4238	−1.6614
SOI	n/a	n/a	n/a	n/a
CR	1.8039	2.9095	−4.689	2.3293
T_{IVC}	1.64	4.9523	−3.214	2.8207

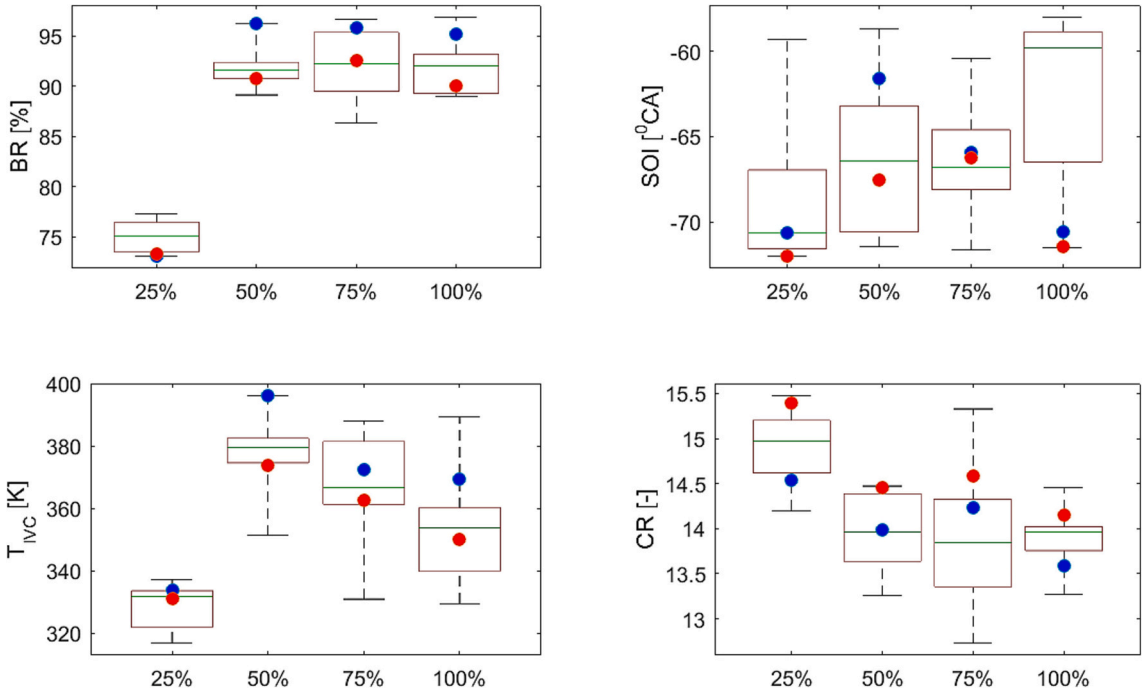

Fig. 7. Box and whisker plot illustrating the region in the design space (factors) resulting in stable combustion across the four load points. The red dots correspond to the best ITE design; blue dots represent the lowest NO_X designs. (For interpretation of the references to colour in this figure legend, the reader is referred to the web version of this article.)

disregarded. Thus, the values in Table 7 are indicative, whereby the relative differences in magnitude and direction (+/−) are relevant.

By observation, T_{IVC} and *CR* are strongly influential. The relationship between responses shows the trade-off between maximising *ITE* while limiting NO_X and P_{max}. NO_X particularly shows high sensitivity to T_{IVC}, due to the thermal formation pathway solely modelled in the chemical mechanism (Section 2.2.1). Mixture dilution (λ), necessary to control NO_X, increases with weakening reactivity (*BR*). This indicates elevated λ is required when operating on a higher proportion of NG in the fuel mixture. λ also demonstrates a negative correlation with T_{IVC} and *CR*. The reason for the former is the connected to desity. On ther other hand, higher λ implies greater air mass flow, which requires lower *CR* to comply with the optimisation constraints.

Fig. 7 uses boxplots of the four factors to illustrates the region within the design space favouring stable combustion for each load point. The underlying data exclude misfire designs from the optimisation run. The green line indicates the median; the upper and lower edges of each box cover the upper and lower quartile, respectively. The whiskers extend to the outliers. Optimum factor values are overlaid, using blue dots for the lowest NO_X design and red dots for the best *ITE* design.

The lower load point requires the mixture to be more reactive than the higher load points. The *BR* range for optimal combustion at 25% load is 73% to 78%. Owing to the low boost levels (1.29–1.37 bar), the max T_{IVC} explored is 337 K at a *CBV* of 45%. Temperatures are insufficient to support high *ITE* (Table 7), so the *CR* is necessarily higher (14.8:1–15.3:1) than for other load points. Moving up to 50% loading, T_{IVC} reaches up to 385 K for a similar opening of *CBV*. Consequently, higher *BR* levels are sustained and are needed to minimise NO_X emissions. At high boost levels (3.75–4.1 bar), as at 100% load point, a *CBV* opening of 18% to 22% results in T_{IVC} with a median around 370 K. This is lower than at 50% and 75% load points. Consequently, *BR* is sufficiently high (93.8% to 95.4%) and median *CR* is around 13.6:1, lower than other points to comply with the NO_X and P_{max} constraints.

3.2.2. Optimum operating conditions

Fig. 8 depicts results corresponding to the best *ITE* and lowest NO_X designs. The top bar plot presents *ITE*, CA50 and λ; the lower one presents *TIT* and emissions of UHC and NO_X. It is evident that the highest λ of 2 is achieved at 25% load, which drops with load to 1.72 at 100% load. Consequently, the lowest NO_X of 1.27 g/kWh is obtained at 25% load, while UHC is highest among all load cases, owing to incomplete combustion, a common problem in RCCI engines [20]. The low-NO_X design of this load point causes UHC as high as 71 g/kWh. Conversely, highest *ITE* of 50.05% is achieved at 75% load, where UHC is the lowest of all at 2.75 g/kWh.

Acknowledging the reciprocal relationship between UHC and *ITE*, the opposing objectives of high *ITE* and low NO_X are evident for all load cases. The low-NO_X designs in Fig. 7 are characterised by higher *BR* and lower *CR*. A higher T_{IVC} is then required due to the lower reactivity. Furthermore, low-NO_X designs for all load cases operate at leaner condition (higher λ), as seen in Fig. 8. All load points, except 100%, potentially satisfy IMO Tier III NO_X limits. However, the requirement of higher *CR* in the best *ITE* designs means they risk violating the constraints on P_{max} and *TIT* at high loads. This challenge is evident at 100% loading, where performance has to be trimmed to comply with the limits. Thus, the best *ITE* at 100% loading is 0.9 pp. lower than that achieved at 75% load.

Fig. 9 depicts the T/C operating condition for the high-*ITE* and low-NO_X designs for all load cases. The compressor map shows that low-NO_X designs demand larger mass flow than the high-*ITE* counterparts, especially for 50%–100% load points. The T/C shaft is driven at a higher speed to satisfy this, as also evident in turbine map. These observations are in line with Fig. 8 for λ. All points are operating with a good margin for surge and choke boundaries. The margin to the choke boundary is 15% at 25% load, whereas the 100% load case is closer to the surge boundary, with a margin of 9.5%, just slightly below the 10% recommendation. The 50% load case is also close to the surge boundary, only 0.1 pp. above the recommended 10%.

3.3. RCCI calibration with hardware-constrained CR

Case study #2 deals with determining a geometric *CR* for the RCCI

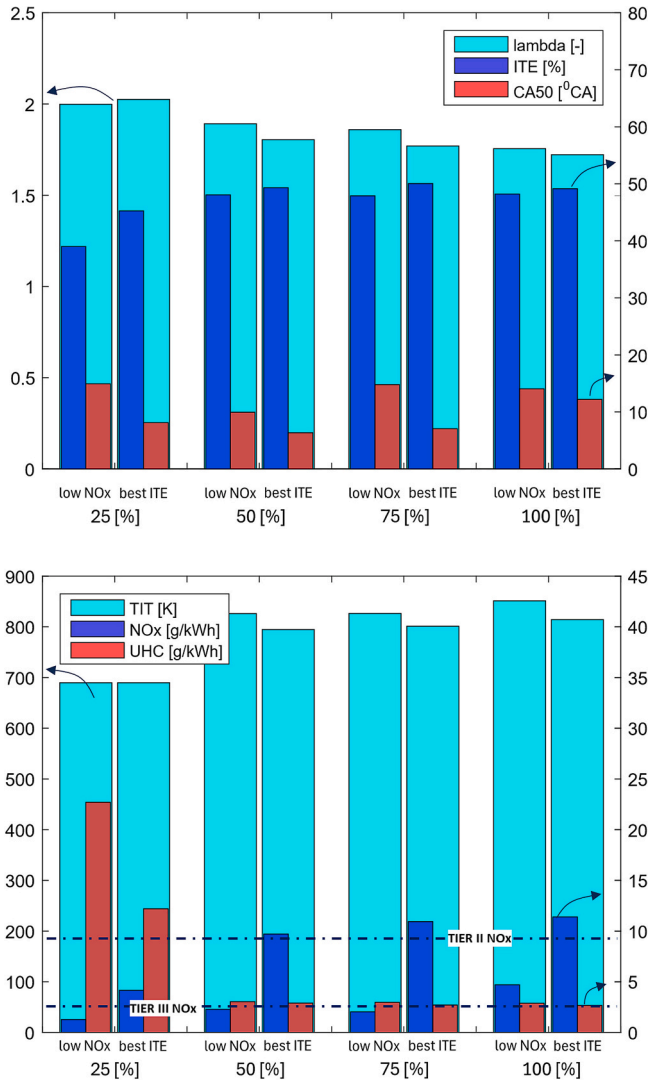

Fig. 8. Responses of the corresponding optima for best ITE and lowest NO_X, for all four load points. Top plot shows λ, ITE and CA50; lower plot shows TIT, NO_X and UHC emissions.

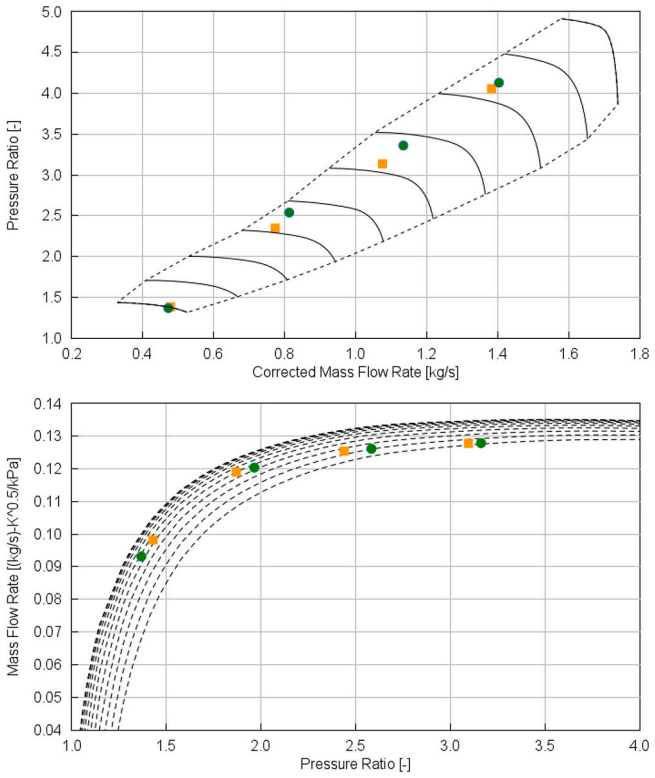

Fig. 9. Turbocharger operating points corresponding to the optimum designs of case study #1 shown on compressor map (top) and turbine map (bottom). The best NO_X designs are shown as green ○ and best ITE designs as orange □. (For interpretation of the references to colour in this figure legend, the reader is referred to the web version of this article.)

Table 8
Weighting factors and optimal CR (load-point-based) from Section 3.2. Weights are taken IMO's NO_X technical code 2008 [54].

Load case [%]	100%	75%	50%	25%
Weights [−]	0.20	0.50	0.15	0.15
Local CR [−]	13.59	14.22	13.34	14.53
Geometric CR [−]	14.01			

retrofit engine and investigating the ensuing performance and operating conditions. Since study #1 included *CR* as a load-point-based factor, those results are used to calculate a geometric *CR*. The approach uses a weighted average, applying the weighting factors in the IMO NO_X technical code [54] for fixed-speed main engines. The weighting factors originally devised to calculate a load-averaged emissions value, are repurposed here (Table 8). The optimal *CR* for the low-NO_X designs from study #1 is in the third row of Table 8. The calculated geometric *CR* is 14.01:1, and will be used further in this study to determine the final engine calibration. The optimiser is then run to maximize ITE_{net}, with constraints on NO_X and P_{max}, and the limits on the design space, listed in Table 5.

Fig. 10 presents the optimum design for each load point, with T_{IVC} directly shown instead of *CBV*. The highest T_{IVC} of 376 K is required at 50% loading, to compensate for the lowered reactivity (*BR* = 92%). T_{IVC} then falls with increasing load. Correspondingly, the SOI at 50% load is the most retarded (58^{0}CA bTDC), facilitating combustion propagation through reactivity stratification. *BR* increases with load, from 73% at low load to 95.05% at full load. The trends here are similar to the previous section's observations (Fig. 7).

The results of these optimal designs are now discussed by comparing them with conventional diesel combustion performance (CDC). Fig. 11

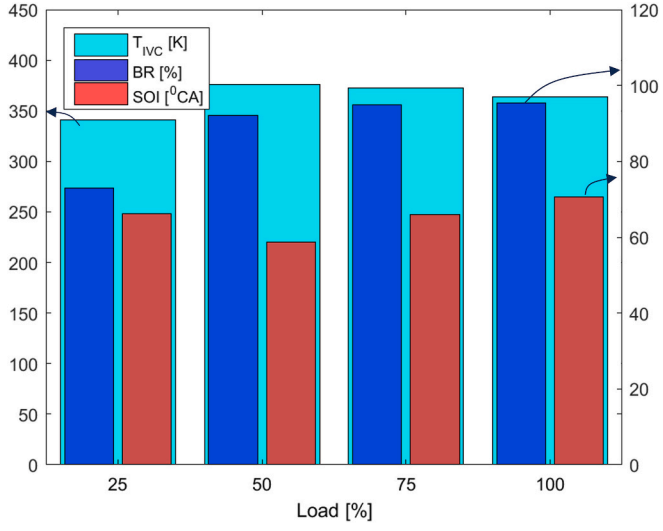

Fig. 10. Optimum parameters of each load point at CR of 14.01:1. The left y-axis relates to T_{IVC}; the right to BR and SOI (^{0}bTDC).

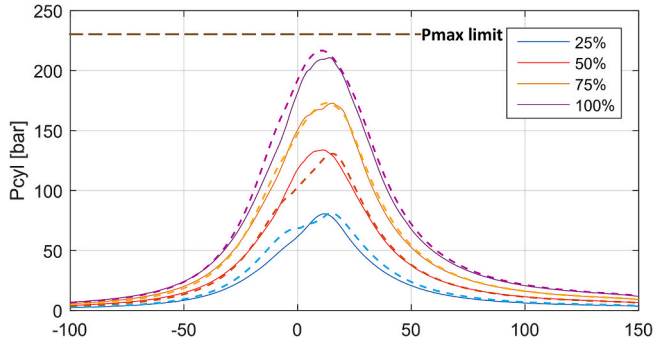

Fig. 11. In-cylinder pressure corresponding to optimal designs of all RCCI load points for CR 14.01:1.

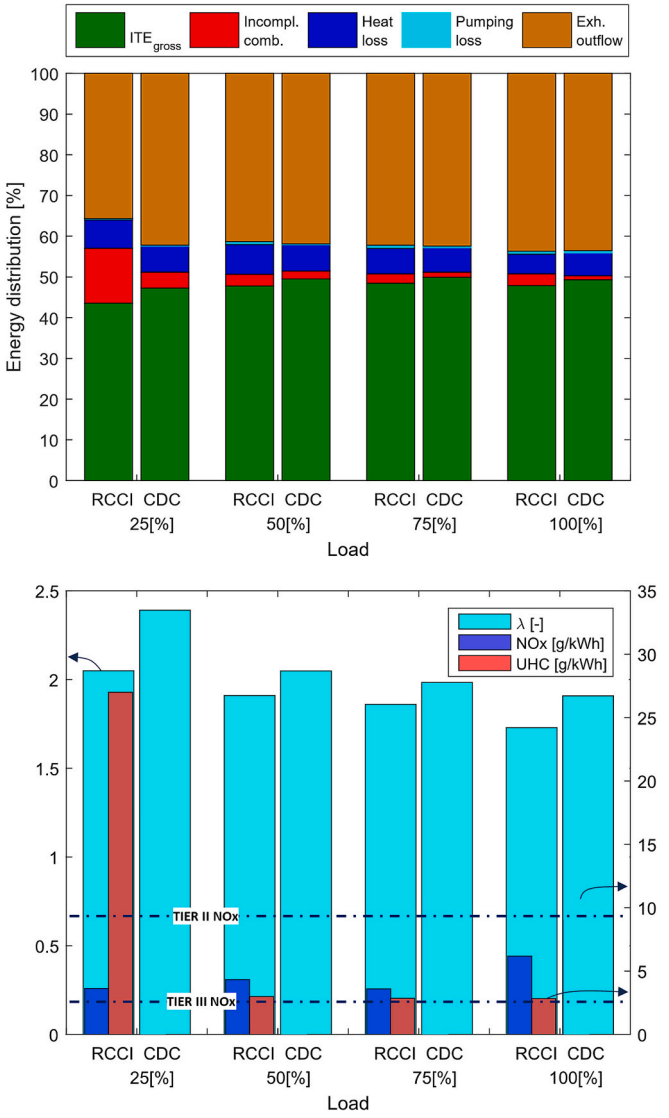

Fig. 12. Results of optimum design at CR 14.01:1. Sankey chart (top) illustrates the different consumers of total fuel energy. The left y-axis of the bar plot (bottom) refers to λ; the right one refers to NO_X and UHC (CH_4 species) emissions.

compares in-cylinder pressure of RCCI and CDC. The P_{max} at 100% load for RCCI is 212 bar, 13 bar shy of the durability limit. The pressure traces look similar but PRR_{max} calculated at full load is 5.82 bar/^{0}CA for RCCI,

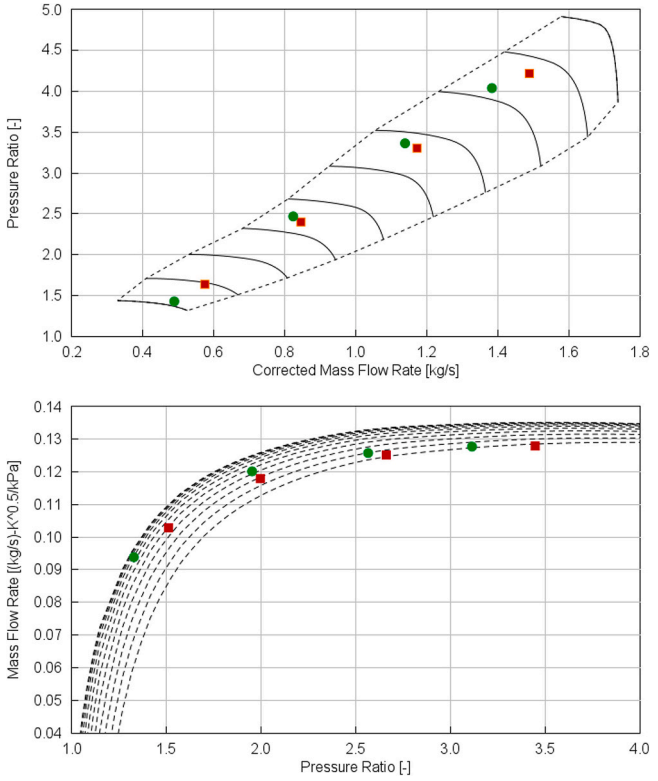

Fig. 13. Turbocharger operating points for the optimum designs of study #2 shown on compressor map (top) and turbine map (bottom). RCCI is denoted by (○) and CDC by (□).

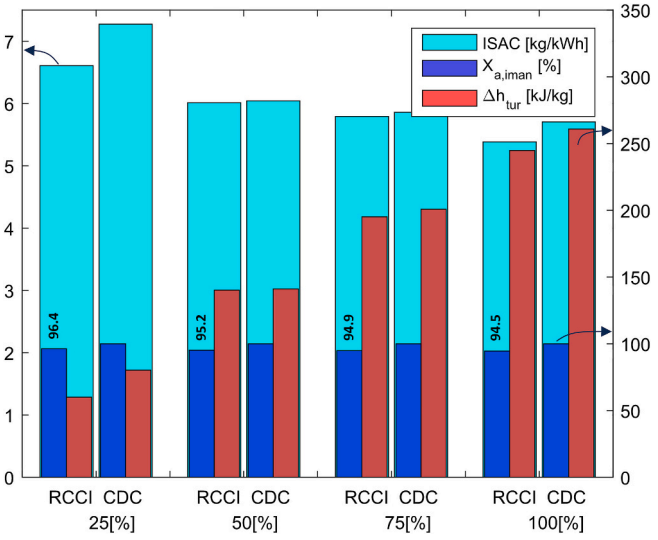

Fig. 14. Comparing T/C performance between RCCI and CDC from case study #2 (CR = 14:1). The parameters are ISAC on the left side y-axis; $X_{a,iman}$ and Δh_{tur} on the right.

5% higher than CDC throughout the load range. The post-processed combustion phasing (CA50) occurs earlier for RCCI by 4^{0}CA at low loading and by 2^{0}CA at high loading. Although not shown, the trend in CA50 for RCCI is monotonic, increasing from 9^{0}CA at 25% loading to 13^{0}CA at full load. CA50 is delayed at high loads to comply with P_{max} limit. However, postprocessed $IMEP_{net}$ for RCCI is lower by 3.5% on average than CDC.

Further insights are obtained from Fig. 12's Sankey plot, where RCCI's

highest *ITE* of 49.4% is achieved at 75% load. This is followed by 48.7% at 100% load, slightly compromised to meet *TIT* and P_{max} limits. These outcomes are similar to (about 0.5 pp. lower) the previous case study's best designs (Fig. 7). However, 25% loading gives the lowest *ITE* of 43%, since the fixed *CR* is below the optimal range (Fig. 7) for this load point, as determined in the previous study. Compared to CDC, the *ITE* for RCCI is lower by 1 pp. for the mid- to high-load cases, while the gap is 4 pp. at 25% loading. This is attributed to poorer combustion efficiency, as seen in Fig. 12. Furthermore, the fraction lost to exhaust is lower by 0.5 pp. in mid- to high-load cases, and by 6 pp. at 25% loading for RCCI, so less energy is available to drive the turbine. The heat-loss fraction is similar for both combustion modes, averaging 5.5%.

Turning to NO_X, none of the RCCI load points is within 2.5 g/kWh (IMO Tier III). The average is 4.4 g/kWh, with the lowest of 3.5 g/kWh at 75% loading, and highest of 6.2 g/kWh at 100% loading. The highest UHC emissions (27.3 g/kWh) are at 25% loading, which is reaffirmed in the Sankey plot, where unburnt fuel energy is about 13%. UHC emissions are about 2.8 g/kWh at the other three load points, translating to about 1.5% fuel energy loss. Emissions measurements were not recorded under CDC mode, so are not shown. However, IMO tier III and II limits are shown for comparison. The production version of Engine B (diesel 200 mm platform) complies with IMO tier II NO_X regulations [41].

The maximum λ from the turbocharger is 2.05 at 25% loading, falling to 1.73 at 100% load, similar to the trend observed in Section 3.2.2. Further insight is obtained from the compressor map (Fig. 13), where peak boost pressure of 4bara is at full load, falling to 1.5bara at low load, in the low-speed region where compressor efficiency drops just below 70%. CDC's λ values are 10% higher on average throughout the load range, because compressor outlet flow for CDC is 8% higher on average than RCCI (Fig. 13). The pressure ratio (PR) for RCCI at 50% and 75% loading is higher than CDC, but yields lower mass flow because the compressor is driven more slowly, as seen in the turbine map.

3.4. Boosting system requirements for optimal RCCI operation

Further insight on the limitations of the stock T/C for RCCI performance are seen in Fig. 14, based on the results of case study #2. First, indicated specific air consumption (ISAC) shows RCCI operating at a lower air flow than baseline CDC. The difference is only 0.5% for the mid-load cases, but grows to 8% for low- and full-load cases. This is reinforced by the λ values in Fig. 12. Furthermore, the RCCI retrofit includes a gas injector in the intake runner. Consequently, the volume flow of air is reduced to accommodate the fuel flow, unlike for CDC. This is indicated by the parameter $X_{a,iman}$ defined in Eq. (1) as volume fraction of air in the fluid flowing through the intake runner. This is undoubtedly unity for CDC, but $X_{a,iman}$ for RCCI is lower, falling from 96.4% at low load to 94.5% at full load as fuelling increases.

$$X_{a,iman} = \frac{\dot{V}_{air}}{\dot{V}_{air} + \dot{V}_{NG}} \times 100 \ \ [\%] \tag{1}$$

Finally, Fig. 14's right y-axis shows the isentropic stagnation enthalpy at the turbine (Δh_{tur}), calculated as Eq. (2), where γ_{eman} is the ratio of specific heats at exhaust manifold conditions, taken as 1.34:1. Broadly, Δh_{tur} is about 9% lower than with CDC. The difference is most evident at low and full loading, similar to the trend in other indicators. Δh_{tur} highlights the lower TIT as a factor in RCCI (due to low-temperature combustion), resulting in less power from the turbine. The untapped performance from RCCI mode is made available when the mixture strength is sufficiently lean ($\lambda > 2$), enabling NO_X to be well within automotive Euro VI's limit [32]. The larger air flow also compensates for the power loss at the crank, making the performance comparable with the baseline diesel engine. For this reason, commercial gas engines are equipped with sequential turbochargers [56].

$$\Delta h_{tur} = c_{p,eman}\ TIT\left[1 - \left(\frac{1}{PR_{tur}}\right)^{\frac{\gamma_{eman}-1}{\gamma_{eman}}}\right] \qquad [kJ/kg] \tag{2}$$

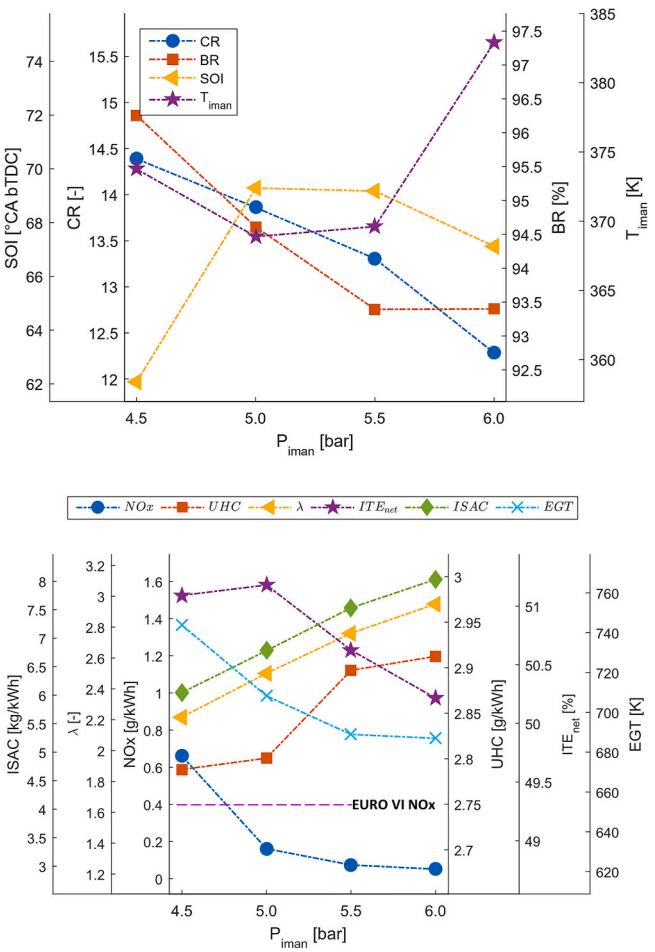

Fig. 15. Optimal factors (top) and the corresponding results (bottom) for each step of boost pressure sweep at 75% loading.

The case for a larger turbo compressor is explored in case study #3. To avoid the complexity of scaling the T/C maps, the model's compressor and turbine components are replaced by fixed boundary conditions representing compressor outlet (P_{iman}, T_{iman}) and turbine inlet (P_{eman}, T_{eman}). The investigation is limited to the 75% load condition. P_{iman}, is swept in discrete steps of 0.5 bar between 4.5 bar and 6 bar. Each step is an optimisation run, i.e., four runs in total, to maximize *ITE*, with T_{iman} along with *BR* and SOI forming the factors. *CR* is also included as the previously determined 14.01:1 will be suboptimal for the higher boost pressures explored. P_{eman} is determined by assuming the same pressure drop across the engine as in the baseline 75% load case. T_{eman} is fixed to 850 K.

Fig. 15's top plot shows the optimum design variables, where *CR* decreases with increasing boost pressure. At P_{iman} of 4.5 bar, 1 bar over the stock T/C delivery, the *CR* is still quite high at 14.5:1. However, it decreases to 13.3:1 at 5.5 bar and 12.3:1 at 6 bar, within the range of *CR* of commercial DF mid-speed engines [38]. *BR* decreases from 96.2% to 93.4%, with P_{iman} indicating the requirement of increased reactivity. This is reinforced by the trend in T_{iman}, which begins to increase after 5 bar, while SOI begins to retard, causing increased HRF stratification. The explanation is in the bottom plot, where λ increases monotonically from 2.2 to 2.9. Thus, at increasingly lean conditions, CA50 (not shown) is maintained between 10^0 and 11^0CA, the optimal range for maximising mean effective pressure. Consequently, *ITE* increases from 51.09% to reach a peak of 51.2% at 5 bar, then reduces, settling at 50.2% at P_{iman} of 6 bar. This peak *ITE* is higher than 50.4% for CDC at the same loading, and 1.16 pp. more than study #1's best *ITE* design.

The increasingly lean conditions produce less NO_X. It is 0.66 g/kWh

at 4.5 bar, already well below IMO Tier III limits. NO_X falls below the automotive Euro VI limit (0.4 g/kWh) at P_{iman} of 5 bar; and goes as low as 0.05 g/kWh at 6 bar. UHC emissions on the other hand increase from 2.78 to 2.9 g/kWh at high boost. The small rate of increase in UHC is corroborated by the high-*ITE* values, sustained despite the lean operation. Importantly, burn duration (not shown) is 25^0CA at λ of 2.9, increasing from 11^0CA through the sweep, while the optimal CA50 hovers around 10^0CA aTDC. The exhaust gas temperature (EGT) correspondingly decreases with P_{iman}. EGT at P_{iman} of 4.5 bar is 40 K lower than the stock T/C conditions. ISAC, like lambda, increases linearly from 6 kg/kWh to 8 kg/kWh. At P_{iman} of 4.5 bar, ISAC is 3.5% greater than with the stock T/C.

Thus, the investigation demonstrates that the retrofit RCCI engine needs a larger T/C to match the power of the baseline diesel that it replaces. This also makes it future-ready by complying with stricter emissions regulations and fuel flexibility. Comprehensive engine-T/C matching is still required, but the indication is for a 22% increase in mass air flow over the stock setup, considering P_{iman} of 5 bar is sufficient at 75% loading. This translates to a 32% increase in the pressure ratio across the compressor, and 17% higher specific air consumption.

4. Conclusions and outlook

The present study extended the UVATZ (University of Vaasa Advanced Thermo-kinetic multi-zone model) mesoscale modelling ecosystem into a full multi-cylinder engine optimisation framework. It provides two complementary advancements: (i) fundamental developments in computational methodology enabling rapid, predictive RCCI simulations (Objective 1); and (ii) demonstrating these capabilities in a technically significant marine retrofit (Objective 2).

4.1. Conclusions

The key takeaways regarding the modelling framework development (Objective 1) are:

- Engine performance is predicted including the histories of in-cylinder pressure, temperature, and the dynamics due to turbocharger. Key performance indicators are predicted within 5% error margin. The more challenging predictions of NO_X and CH_4 emissions are achieved within 35% error margin.
- Although based on chemical kinetics, the model is computationally light, allowing large-scale optimisation runs. This is demonstrated over 12 optimisation cases with up to five factors, totalling 1880 design iterations. Each converged simulation requires under 25 min.

The important outcomes regarding the framework's application towards designing a new multi-cylinder RCCI marine engine (Objective 2) are:

- Charge-air temperature regulation via an intercooler-bypass valve is shown to be an effective means of controlling combustion phasing and suppressing NO_X formation across the entire load range.
- Optimising compression ratio (*CR*) underscores the trade-off between efficiency and NO_X emissions. Best-point indicated thermal efficiency (*ITE*) of 50.05% is shown for 75% loading at *CR* of 14.6:1. A slight decrease in *CR* to 14.2:1 shows NO_X as low as 2.03 g/kWh (<IMO Tier III) achievable at the same load point, but compromising *ITE* by 2.2 percentage points
- With the stock turbocharger, the minimum average NO_X emissions of 4.2 g/kWh (half of IMO Tier II limit) is achieved across the load range for *CR* optimised to 14.01:1. CH_4 emission is 2.9 g/kWh on average from 50% to 100% load points. However, a large value is predicted at 25% loading, necessitating a methane oxidation catalyst aftertreatment. The highest *ITE* of 49.4% is achieved at 75% load, operating with the natural-gas energy share of 95%. The optimum points operate within the constraints of peak cylinder pressure below 225 bar and exhaust-gas temperature below 850 K.
- Owing to the reduced (9%) turbine inlet enthalpy and lower (5%) volumetric efficiency in port fuel injected RCCI than in diesel mode, the resulting *ITE* is also 1 percentage point below diesel's performance. Therefore, optimising the air management system holds the key to unlock RCCI's *ITE* to 51.2%, with NO_X emissions of 0.16 g/kWh, well below the automotive Euro VI limit, as demonstrated for 75% loading. This translates to the specific air-demand approximately 17% over the stock turbocharger's capacity.

4.2. Outlook

Before the application of the simulation framework towards the broader objective of accelerating adoption of RCCI technology, there are few shortcomings that need to be matured. The most important are identified as follows:

- Fuel stratification model: Since it is of response-surface type, based on CFD spray simulations, the predictions are bounded by the limits of the training data. Thus, SOI in this research is restricted to 58° – 72 °CA bTDC, and *BR* below 73% is not explored. To overcome this, a higher fidelity approach, similar to Musculus and Kattke's [57] 1D spray model, has been developed within the research group [58], and is currently being coupled to UVATZ.
- Methodology improvement: The study campaign on boosting system requirement, as described in Section 3.4, is a simplified analysis wherein the turbocharger submodel is decoupled. Therefore, a follow-up study shall comprehensively cover the topic, encompassing turbocharger matching and covering whole load range.
- Validation of the optima: The results from this study are the first step in justifying expenditure to conduct a retrofit of the laboratory engine (Wärtsilä 4L20). While the first set of results from this engine are published [59], a follow-up study shall be dedicated to implement the optimum designs proposed here, ultimately validating the predictions.

Declaration of generative AI in scientific writing

The authors declare that no generative AI and AI-assisted technologies were used in the writing process.

CRediT authorship contribution statement

Aneesh Vasudev: Writing – original draft, Visualization, Software, Methodology, Investigation, Formal analysis, Data curation, Conceptualization. **Jeyoung Kim:** Writing – original draft, Visualization, Validation, Software, Methodology, Formal analysis, Data curation. **Kian Golbaghi:** Writing – original draft, Software, Methodology, Investigation, Formal analysis, Data curation. **Martin Axelsson:** Writing – review & editing, Writing – original draft, Resources, Data curation. **Ben Smulter:** Writing – review & editing, Resources, Data curation. **Jari Hyvönen:** Writing – review & editing, Supervision, Resources. **Maciej Mikulski:** Writing – review & editing, Supervision, Resources, Project administration, Methodology, Funding acquisition, Conceptualization.

Declaration of competing interest

The authors declare the following financial interests/personal relationships which may be considered as potential competing interests: Aneesh Vasudev reports financial support was provided by Business Finland. If there are other authors, they declare that they have no known competing financial interests or personal relationships that could have appeared to influence the work reported in this paper.

Acknowledgements

The work was conducted within the Wärtsilä ZEM (zero emission marine) ecosystem, with financial support provided by Business Finland through CASEMATE project (Ref. 2911/31/2022). The authors also appreciate the invaluable contribution of Mr. David Wilcox in proof-reading our manuscript and providing his expert suggestions on stylistic points.

Appendix A. Postprocessing routine

The raw output data from the simulation contain the thermodynamic state of each zone including their individual composition histories. Since all zones share a common pressure, the in-cylinder pressure is taken as any one of the zone's pressure. The raw pressure data exhibits jagged features, inherent to such multizone approaches [60]. Hence, a simple moving average filter is applied to smooth it. The pressure rise rate (*PRR*) is then computed as bar/^{0}CA by applying a Savitzky-Golay filter: PRR_{max} is determined from the peak value. Furthermore, heat release rate (*HRR*) during the cycle is calculated via the apparent heat release approach (Eq. (3)) from the simulated pressure curve. The ratio of specific heats (γ) used here is fixed to 1.368, based on the setup calibration.

$$HRR_{net} = \left(\frac{\gamma}{\gamma-1}\right) P \frac{dV}{d\theta_{CA}} + \left(\frac{1}{\gamma-1}\right) V \frac{dP}{d\theta_{CA}} \qquad \left[J/^0CA\right] \tag{3}$$

Additionally, typical engine performance indicators are also postprocessed. First, the quantity of net heat released (*NHR*) is computed as the integral of HRR over the closed cycle. A cumulative integral on *HRR* provides the cumulative heat release (*CHR*) profile. Combustion phasing indicators, i.e., CA50, CA10, and burn duration (CA10–90) are determined from CHR.

The indicated mean effective pressure (Eq. (4)) is an engine-size independent quantifier of applied load, and is calculated over the full cycle (720^{0}CA) from in-cylinder pressure. Pumping mean effective pressure (*PMEP*) is computed using the same relation, but integrated only over the duration, exhaust valve opening (EVO) to IVC. Based on mean effective pressure, the net indicated thermal efficiency (ITE_{net}) is computed as in Eq. (5). The fuel flow rate ($\dot{m}_{LRF}$,$\dot{m}_{HRF}$) of the LRF and HRF, combined with their heating value (LHV), gives the available fuel power. V_{disp} is displacement in m^3 and N_{eng} is engine speed in rev/s. Additionally, the pumping loss, i.e., the fraction of fuel energy used for powering the open part of the cycle, is also calculated from Eq. (5), but replacing IMEP with PMEP.

$$IMEP_{net} = \frac{1}{V_{disp}} \oint P\, dV \qquad [bar] \tag{4}$$

$$ITE_{net} = \frac{1/2 \cdot IMEP_{net} \cdot V_{disp} \cdot N_{eng}}{\dot{m}_{LRF} LHV_{LRF} + \dot{m}_{HRF} LHV_{HRF}} \text{ x100} \qquad [\%] \tag{5}$$

Combustion performance is quantified by the incomplete combustion loss (CL), which is a fraction of fuel energy. Eq. (6) uses the energy contained within the emission species of CH_4, CO and non-methane hydrocarbon (NMHC). The lower heating value (LHV) of CO is taken as 10.1 J/kg, while that for NMHC assumes the same as LFO. Finally, calculation of indicated specific quantities is represented as a generalised expression, Eq. (7), where *x* can be emissions (NO_X or UHC) or fuel consumption. The unit is g/kWh, when the associated mass flow is expressed in g/h and $IMEP_{net}$ as kPa.

$$CL = \frac{\dot{m}_{exh}(Y_{CH4} LHV_{CH4} + Y_{CO} LHV_{CO} + Y_{NMHC} LHV_{LFO})|_{\theta=EVO}}{\dot{m}_{LRF} LHV_{LRF} + \dot{m}_{HRF} LHV_{HRF}} \text{ x100} \qquad [\%] \tag{6}$$

$$ISx = \frac{2 \cdot \dot{m}_x}{IMEP_{net} \cdot V_{disp} \cdot N_{eng}} \qquad [g/kWh] \tag{7}$$

Note, that the methodology described here is consistently applied to postprocess both simulation and experimental data. This is done to secure model validation results.

Appendix B. Model equations

B.1. Fundamental balance equations

The governing equations of UVATZ are based on the balance of mass and energy in a network of homogeneous reactors. The mass balance equation (Eq. (8)) is shown for a zone 'z' considering the closed part of the four-stroke cycle. The mass flow across the boundaries constitutes the direct injected HRF fuel as the first term. The second term corresponds to the flow from the neighbouring zones as a result of interzonal turbulent mixing. It is assumed that the positive direction of flow occurs from innermost to outermost zone. The subscript *i* is the chemical species index.

$$\frac{dm_z}{dt} = \dot{m}_{inj,z} + \sum\nolimits_i \left(\dot{m}_{i,z-1\to z} - \dot{m}_{i,z\to z+1}\right) \tag{8}$$

The energy balance for each zone is given in Eq. (9), wherein the terms on the left correspond to the overall change in internal energy of the reactor z. The first term on the right corresponds to boundary work on the reactor, which includes contributions from both piston motion and movement of the interzonal boundaries. The second term corresponds to the heat exchanged to the environment from the combustion chamber surfaces. The third term is associated with the evaporation enthalpy of the injected fuel. The heat flow from the neighbouring zones as a result of turbulent mixing is captured by the fourth and fifth group of terms, from diffusion-based transport and advection respectively.

$$m_z c_{v,z} \frac{dT_z}{dt} + \left(u_z \frac{dm_z}{dt} + m_z \sum\nolimits_i u_{i,z} \frac{dY_{i,z}}{dt}\right) = -P_{cyl} \frac{dV_z}{dt} - \dot{Q}_{HL,z} - \dot{m}_{inj,z} q_{evp,z} + (\dot{Q}_{z-1\to z} - \dot{Q}_{z\to z+1}) + \left(h_{z-1} \sum\nolimits_i \dot{m}_{i,z-1\to z} - h_z \sum\nolimits_i \dot{m}_{i,z\to z+1}\right) \tag{9}$$

Eq. (10) provides the balance equation for chemical species in each zone. The contribution from chemical reactions is captured in the first term on the right. $\dot{\omega}_i$ is the net production rate of species *i*, evaluated from the rate of chemical reactions in Cantera [48]. The composition change due to mass

flow across the boundaries is captured in the terms that follow. The injected high reactivity fuel is represented in the third term, while the last corresponds to the contribution from interzonal mass flow.

$$\left(m_z\frac{dY_{i,z}}{dt}+Y_i\frac{dm_z}{dt}\right)=\frac{\dot{\omega}_{i,z}W_{i,z}}{\rho_z}+\dot{m}_{z,inj}Y_{diesel}+\left(\dot{m}_{i,z-1\to z}-\dot{m}_{i,z\to z+1}\right) \tag{10}$$

The system of equation is closed by using the equation of state (Eq. (11)). Since it is assumed that all zones share a common pressure (P_{cyl}) the constraint on the zone volume Eq. (12) is imposed. $\overline{W}_z$ is the average molecular weight based on the composition in zone z.

$$P_{cyl}V_z=m_z\frac{R_u}{\overline{W}_z}T_z \tag{11}$$

$$\sum_z^{nZ}V_z=V_{cyl} \tag{12}$$

B.2. Submodels

B.2.1. Heat loss to environment.

In the energy equation (Eq. (9)), heat exchanged with environment is modelled as Eq. (13). Here A_{surf} is the heat exchange surface area with reactor z, with T_{wall} being the corresponding surface temperature. Table 3 provides the wall surface temperatures of piston, head and liner. h_z is the convective heat transfer coefficient determined by the correlation from Chang et al. [45], based on the thermodynamic state of the individual zones (Table 2).

$$\dot{Q}_{HL,z}=h_z\,A_{surf,z}\,(T_z-T_{wall}) \tag{13}$$

B.2.2. Interzonal heat and mass transport

With the assumptions of in-cylinder flow being axisymmetric, and all zones sharing the same pressure as the cylinder, the flow of heat and mass is considered in the radial direction. In order to capture the phenomenon of turbulent mixing, the flow of heat and mass is assumed to be driven by the interzonal gradient of temperature and concentration, respectively. Eqs. (14) and (15), show the fluxes for mass and heat between zones z and z + 1, with ΔT / Δw being the temperature gradient and ρΔY$_i$ / Δw being the concentration gradient of species i. The coefficient Λ is thermal conductivity and D is molecular diffusivity. The latter is obtained via the unity Lewis assumption (Table 2). ${}^{M}\zeta_t$ and ${}^{H}\zeta_t$ are the mixing intensity enhancing factors for applied on the diffusion coefficients of mass and heat respectively.

$$\dot{m}_{i,z\to z+1}=\begin{cases}{}^{M}\zeta_t\left(\mathfrak{D}\rho\dfrac{\Delta Y_i}{\Delta w}\right)_{z\to z+1} & i\neq\text{HRF}\\ 0 & i=\text{HRF}\end{cases} \tag{14}$$

$$\dot{Q}_{z\to z+1}={}^{H}\zeta_t\left(\Lambda\frac{\Delta T}{\Delta w}\right)_{z\to z+1} \tag{15}$$

The interzonal mixing intensity factors are from the 0-dimensional turbulence model [44] which is based on the turbulence energy cascade mechanism. By using turbulent Schmidt (Sc_t) and Prandtl (Pr_t) numbers, a relationship is formed with ${}^{M}\zeta_t$ and ${}^{H}\zeta_t$, respectively, as shown in Eqs. (16) and (17). The basis for this relationship is derived from the assumption that the effective values of heat diffusivity and thermal conductivity are the sum of the molecular and turbulent components, Eqs. (18) and (19), respectively. For simulations, Sc_t and Pr_t are assumed unity. Readers are directed to the work [44] for details on the turbulence energy cascade model.

$${}^{M}\zeta_t=\frac{\mathfrak{D}_e}{\mathfrak{D}}=1+\frac{1}{\mathfrak{D}}\frac{\vartheta_t}{Sc_t} \tag{16}$$

$${}^{H}\zeta_t=\frac{\Lambda_e}{\Lambda}=1+\frac{1}{\Lambda}\frac{c_P\rho\vartheta_t}{Pr_t} \tag{17}$$

$$\mathfrak{D}_e=\mathfrak{D}+\mathfrak{D}_t \tag{18}$$

$$\Lambda_e=\Lambda+\Lambda_t \tag{19}$$

B.2.3. HRF stratification

The decoupled nature of injection and combustion phasing in RCCI [19] allows the HRF spray phenomenon to be modelled in a simplified manner. Thus, details of the spray development process may be disregarded, with focus shifted directly to the ensuing bulk in-cylinder stratification which triggers combustion. With the spray emanating from a multi-hole injector, it is assumed that the bulk fuel inhomogeneity nearing start of combustion (SOC) is in the radial direction of the cylinder. As such, the HRF in UVATZ is directly injected as vapour into the annular zones (2−10) according to a predetermined profile at the moment of SOI. The enthalpy of evaporation is simply accounted for as proportional to the injected fuel mass in each zone.

The injected fuel mass follows a profile (Eq. (20)) where the richest fuel equivalence ratio (${}^{HEF}\lambda$) region is located at the liner zone. This follows from observation of CFD spray simulations conducted in the earlier work [39] of the authors. ${}^{HRF}\lambda_{10}$ is fuel equivalence ratio in the 10th zone and is determined from the correlation in Eq. (21). This correlation includes the factors of density at IVC (ρ_{IVC}), injected HRF mass (m_{HRF}) and injection

timing (*SOI*). A response surface approach was used to develop this by postprocessing CFD spray simulations [39], thus the hat represents that the factors were normalised to their respective limit values. ζ_{∇} is the exponent of profile (Eq. (20)), and is determined by setting the relation i.e., ${}^{HEF}\lambda_z$, to infinity at z = 2. This implies that zones 3 to 10 are seeded with HRF.

$${}^{HEF}\lambda_z = {}^{HRF}\lambda_{10} \cdot 10^{\zeta_{\nabla}(10-z)} \qquad z = 3 \ldots 9 \tag{20}$$

$${}^{HRF}\lambda_{10} = 3.25 + 1.17 \cdot \widehat{SOI} - 1.626 \cdot \hat{m}_{HRF} - 0.799 \cdot \hat{\rho}_{IVC} - \; - 0.177 \cdot \widehat{SOI} \cdot \hat{m}_{HRF} - 0.713 \cdot \widehat{SOI} \cdot \hat{\rho}_{IVC} + 0.971 \cdot \hat{\rho}_{IVC} \cdot \hat{m}_{HRF} + 0.333 \cdot \widehat{SOI} \cdot \hat{m}_{HRF} \cdot \hat{\rho}_{IVC} \tag{21}$$

Data availability

Data will be made available on request.

References

[1] L. Čampara, N. Hasanspahić, S. Vujičić, Overview of MARPOL ANNEX VI regulations for prevention of air pollution from marine diesel engines, SHS Web Conf. (2018) 58, https://doi.org/10.1051/shsconf/20185801004.

[2] E. Ovrum, T. Longva, L.S. Hammer, N.H. Rivedal, Ø. Endresen, M.S. Eide, Maritime Forecast to 2050, DNV, Norway, 2022.

[3] J. Deng, X. Wang, Z. Wei, L. Wang, C. Wang, Z. Chen, A review of NOx and SOx emission reduction technologies for marine diesel engines and the potential evaluation of liquefied natural gas fuelled vessels, Sci. Total Environ. 766 (2021) 144319, https://doi.org/10.1016/j.scitotenv.2020.144319.

[4] A. Arnberger, S. Golini, D. Mumford, G. Hasenbichler, Commercial natural gas vehicles: Tomorrow's engine technologies for most stringent NOx and CO2 targets, in: J. Liebl, C. Beidl, W. Maus (Eds.), Internationaler Motorenkongress 2018, Springer Fachmedien Wiesbaden, Wiesbaden, 2018, pp. 315–338.

[5] K. Takasaki, Observations on the development and practical application of marine gas engines, ClassNK Technical Bulletin 30 (2012) 1–9.

[6] X. Yang, Y. Cheng, P. Wang, The scavenging timing of pre-chamber on the performance of a natural gas engine, Int. J. Engine Res. 22 (2021) 2919–2930, https://doi.org/10.1177/1468087420960876.

[7] C.E.C. Alvarez, G.E. Couto, V.R. Roso, A.B. Thiriet, R.M. Valle, A review of prechamber ignition systems as lean combustion technology for SI engines, Appl. Therm. Eng. 128 (2018) 107–120, https://doi.org/10.1016/j.applthermaleng.2017.08.118.

[8] C. Hall, M. Kassa, Advances in combustion control for natural gas–diesel dual fuel compression ignition engines in automotive applications: a review, Renew. Sust. Energ. Rev. 148 (2021) 111291, https://doi.org/10.1016/j.rser.2021.111291.

[9] L. Wei, P. Geng, A review on natural gas/diesel dual fuel combustion, emissions and performance, Fuel Process. Technol. 142 (2016) 264–278, https://doi.org/10.1016/j.fuproc.2015.09.018.

[10] A. Boretti, Advances in diesel-LNG internal combustion engines, Appl. Sci. (Basel) 10 (2020), https://doi.org/10.3390/app10041296.

[11] V.B. Pedrozo, X. Wang, W. Guan, H. Zhao, The effects of natural gas composition on conventional dual-fuel and reactivity-controlled compression ignition combustion in a heavy-duty diesel engine, Int. J. Engine Res. 23 (2022) 397–415, https://doi.org/10.1177/1468087420984044.

[12] S.J. Curran, R.M. Hanson, R.M. Wagner, Reactivity controlled compression ignition combustion on a multi-cylinder light-duty diesel engine, Int. J. Engine Res. 13 (2012) 216–225, https://doi.org/10.1177/1468087412442324.

[13] J. Benajes, A. García, J. Monsalve-Serrano, I. Balloul, G. Pradel, Evaluating the reactivity controlled compression ignition operating range limits in a high-compression ratio medium-duty diesel engine fueled with biodiesel and ethanol, Int. J. Engine Res. 18 (2017) 66–80, https://doi.org/10.1177/1468087416678500.

[14] N. Ganesan, T.H. Le, P. Ekambaram, D. Balasubramanian, V.V. Le, A.T. Hoang, Experimental assessment on performance and combustion behaviors of reactivity-controlled compression ignition engine operated by n-pentanol and cottonseed biodiesel, J. Clean. Prod. 330 (2022) 129781, https://doi.org/10.1016/j.jclepro.2021.129781.

[15] E. Doosje, F. Willems, R. Baert, Experimental demonstration of RCCI in heavy-duty engines using diesel and natural gas, SAE Int. (2014), https://doi.org/10.4271/2014-01-1318.

[16] R.M. Hanson, S.L. Kokjohn, D.A. Splitter, R.D. Reitz, An experimental investigation of fuel reactivity controlled PCCI combustion in a heavy-duty engine, SAE Int. (2010), https://doi.org/10.4271/2010-01-0864.

[17] D. Splitter, R.D. Reitz, R. Hanson, High efficiency, low emissions RCCI combustion by use of a fuel additive, SAE Int J Fuels Lubr 3 (2010) 742–756, https://doi.org/10.4271/2010-01-2167.

[18] M. Mikulski, T. Ovaska, R. Rabetino, M. Kangasjärvi, A. Myllykangas, Clean propulsion technologies: Securing technological dominance for the Finnish marine and off-road powertrain sectors, Energies 18 (2025), https://doi.org/10.3390/en18051240.

[19] A. Paykani, A. Garcia, M. Shahbakhti, P. Rahnama, R.D. Reitz, Reactivity controlled compression ignition engine: pathways towards commercial viability, Appl. Energy 282 (2021) 116174, https://doi.org/10.1016/j.apenergy.2020.116174.

[20] M. Mikulski, P.R. Balakrishnan, E. Doosje, C. Bekdemir, Variable valve actuation strategies for better efficiency load range and thermal management in an RCCI engine, 2018, https://doi.org/10.4271/2018-01-0254.

[21] M. Mikulski, C. Bekdemir, Understanding the role of low reactivity fuel stratification in a dual fuel RCCI engine – a simulation study, Appl. Energy 191 (2017) 689–708, https://doi.org/10.1016/j.apenergy.2017.01.080.

[22] C. Atkinson, Fuel efficiency optimization using rapid transient engine calibration, SAE Int. (2014), https://doi.org/10.4271/2014-01-2359.

[23] A. Indrajuana, C. Bekdemir, X. Luo, F. Willems, Robust multivariable feedback control of natural gas-diesel RCCI combustion, IFAC-PapersOnLine 49 (2016) 217–222, https://doi.org/10.1016/j.ifacol.2016.08.033.

[24] D. Morandotti, A. Pelosi, Toward Digital Twin and Simulation- Driven New Product Development, Italy, 2018.

[25] P. Schneider, C. Bayer, K. Einwich, A. Köhler, System Level Simulation — A Core Method for Efficient Design of MEMS and Mechatronic Systems, IEEE, Germany, 2012, pp. 1–6, https://doi.org/10.1109/SSD.2012.6198066.

[26] E. Ansari, M. Shahbakhti, J. Naber, Optimization of performance and operational cost for a dual mode diesel-natural gas RCCI and diesel combustion engine, Appl. Energy 231 (2018) 549–561, https://doi.org/10.1016/j.apenergy.2018.09.040.

[27] X. Ao, H. Gan, M. Xin, Y. Cong, D. Lu, A. Guo, H. Wang, Numerical investigation on the effects of pilot fuel and natural gas injection pressures on methane slip in a large marine dual-fuel engine, Energy 312 (2024) 133675, https://doi.org/10.1016/j.energy.2024.133675.

[28] S.-J. Jeong, S. Seo, S.-J. Moon, CFD simulation of pre-chamber spark-ignition large bore CNG engine: model development, practical applications, and experimental validation, Energies 18 (2025), https://doi.org/10.3390/en18071600.

[29] Y. Cong, H. Gan, H. Wang, G. Hu, Y. Liu, Multiobjective optimization of the performance and emissions of a large low-speed dual-fuel marine engine based on MNLR-MOPSO, J. Mar. Sci. Eng. 9 (2021) 1170, https://doi.org/10.3390/jmse9111170.

[30] J. Park, K.S. Lee, M.S. Kim, D. Jung, Numerical analysis of a dual-fueled CI (compression ignition) engine using latin hypercube sampling and multi-objective pareto optimization, Energy 70 (2014) 278–287, https://doi.org/10.1016/j.energy.2014.03.122.

[31] A. Modabberian, X. Storm, A.-M. Shamekhi, A. Vasudev, K. Zenger, J. Hyvönen, M. Mikulski, Low temperature combustion modeling and predictive control of marine engines, Appl. Sci. 14 (2024), https://doi.org/10.3390/app14052033.

[32] M. Mikulski, S. Ramesh, C. Bekdemir, Reactivity controlled compression ignition for clean and efficient ship propulsion, Energy 182 (2019) 1173–1192, https://doi.org/10.1016/j.energy.2019.06.091.

[33] Flexible Clean Propulsion Technologies, Flexible Clean Propulsion Technologies 2024. https://cleanpropulsion.org/, 2024.

[34] CASEMATE - Computationally Aided Systems Engineering for Marine Advanced Technology for tThe Environment. University of Vaasa. https://www.uwasa.fi/fi/tutkimus/hankkeet/casemate-computationally-aided-systems-engineering-marine-advanced-technology, 2023 (accessed August 12, 2021).

[35] A. Kakoee, J. Hunicz, M. Mikulski, Integrated 1D simulation of aftertreatment system and chemistry-based multizone RCCI combustion for optimal performance with methane oxidation catalyst, J. Mar. Sci. Eng. 12 (2024), https://doi.org/10.3390/jmse12040594.

[36] J. Kim, A. Kakoee, J. Hyvönen, M. Mikulski, Variable valve actuation enabled reactivity- controlled compression ignition in a natural-gas/diesel marine engine, in: THIESEL 2024 Conference on Thermo- and Fluid Dynamics of Clean Propulsion Powerplants, University of Valencia, Spain, 2024. https://doi.org/10.13140/RG.2.2.27266.39362.

[37] A. Vasudev, A. Soleimani, J. Hyvönen, M. Mikulski, Feasible route towards decarbonising marine transport with flexible, hydrogen – enriched, reactivity controlled compression ignition mid-speed engines, Int. J. Hydrog. Energy 142 (2025) 1196–1210, https://doi.org/10.1016/j.ijhydene.2025.02.152.

[38] Wärtsilä 20DF Product Guide, Wärtsilä, Marine Solutions, Vaasa, Finland, 2024.

[39] A. Vasudev, A. Kakoee, M. Axelsson, H.M. Almani, J. Hyvönen, M. Mikulski, Advancing autonomy of chemical kinetics based multizone models for reactivity controlled compression ignition engines, Energy Convers. Manag. 312 (2024) 118562, https://doi.org/10.1016/j.enconman.2024.118562.

[40] S. Hautala, M. Mikulski, E. Söderäng, X. Storm, S. Niemi, Toward a digital twin of a mid-speed marine engine: from detailed 1D engine model to real-time implementation on a target platform, Int. J. Engine Res. 24 (2023) 4553–4571, https://doi.org/10.1177/14680874221106168.

[41] Wärtsilä 20 Product Guide, Wärtsilä Marine Solutions, Vaasa, Finland, 2015.

[42] K. Wells, A. Sharifian, Design of short venturi flow meters for incompressible and isothermal flow applications, Heliyon 10 (2024), https://doi.org/10.1016/j.heliyon.2024.e29311.

[43] A. Vasudev, A. Cafari, M. Axelsson, M. Mikulski, J. Hyvönen, Towards next generation control-oriented Thermo-kinetic model for reactivity controlled compression ignition marine engines, SAE (2022), https://doi.org/10.4271/2022-01-1033.
[44] F. Bozza, L. Teodosio, V. De Bellis, S. Fontanesi, A. Iorio, A refined OD turbulence model to predict tumble and turbulence in SI engines, SAE Int. J. Engines 12 (2019) 15–30.
[45] J. Chang, O. Güralp, Z. Filipi, D. Assanis, T.-W. Kuo, P. Najt, R. Rask, New heat transfer correlation for an HCCI engine derived from measurements of instantaneous surface heat flux, SAE Trans., Section 3: J. Engines 113 (2004) 1576–1593.
[46] T. Yao, Y. Pei, B.-J. Zhong, S. Som, T. Lu, K.H. Luo, A compact skeletal mechanism for n-dodecane with optimized semi-global low-temperature chemistry for diesel engine simulations, Fuel 191 (2017) 339–349, https://doi.org/10.1016/j.fuel.2016.11.083.
[47] Y. Sun, R. Reitz, Modeling diesel engine NOx and soot reduction with optimized two-stage combustion, SAE Int. (2006), https://doi.org/10.4271/2006-01-0027.
[48] D.G. Goodwin, H.K. Moffat, R.L. Speth, Cantera: an Object-Oriented Software Toolkit for Chemical Kinetics, Thermodynamics, and Transport Processes, Version 2.4.0, 2018, https://doi.org/10.5281/zenodo.170284.
[49] A. Kakoee, A. Vasudev, B. Smulter, J. Hyvönen, M. Mikulski, A predictive 1-D modelling framework for reactivity-controlled compression ignition engine via chemistry based multi-zone model, SAE Int. (2023), https://doi.org/10.4271/2023-24-0001.
[50] S.D. Cohen, A.C. Hindmarsh, P.F. Dubois, CVODE, a stiff/nonstiff ODE solver in c, Comput. Phys. 10 (1996) 138.
[51] M. Mohamed Ibrahim, A. Ramesh, Investigations on the effects of intake temperature and charge dilution in a hydrogen fueled HCCI engine, Int. J. Hydrog. Energy 39 (2014) 14097–14108, https://doi.org/10.1016/j.ijhydene.2014.07.019.
[52] M. Herranen, Fully Variable Valve Actuation in Large Bore Diesel Engines. PhD Thesis, Tampere University of Technology, 2014.
[53] Functional Mock-up Interface for Model Exchange and Co-Simulation 2014.
[54] Resolution MEPC.177(58) Amendments to the Technical Code on Control of Emissions of Nitrogen Oxides from Marine Diesel Engines (NOx Technical Code 2008) 2008.
[55] H.M. Cho, B.-Q. He, Spark ignition natural gas engines—a review, Energy Convers. Manag. 48 (2007) 608–618, https://doi.org/10.1016/j.enconman.2006.05.023.
[56] S. Stoumpos, G. Theotokatos, E. Boulougouris, D. Vassalos, I. Lazakis, G. Livanos, Marine dual fuel engine modelling and parametric investigation of engine settings effect on performance-emissions trade-offs, Ocean Eng. 157 (2018) 376–386, https://doi.org/10.1016/j.oceaneng.2018.03.059.
[57] M.P.B. Musculus, K. Kattke, Entrainment waves in diesel jets, SAE Int. J. Engines 2 (2009) 1170–1193.
[58] S. Heidarabadi, H. Maleki Almani, A. Kakoee, A. Andwari, J. Hyvönen, M. Mikulski, Development of a phenomenological spray model for next generation dual-fuel marine engines: validation in free-field conditions, Fuel (2025). Available at SSRN: https://ssrn.com/abstract=6246698.
[59] J. Kim, J. Hyvönen, M. Mikulski, Variable valve actuation-enabled reactivity-controlled compression ignition in a medium speed marine engine: An experimental study, in: In: 15th Asia-Pacific Conference on Combustion (ASPACC 2025), Singapore, 2025. Available at: https://cleanpropulsion.org/wp-content/uploads/2025/05/ASPACC_2025_v15-2.pdf.
[60] A. Vasudev, M. Mikulski, P.R. Balakrishnan, X. Storm, J. Hunicz, Thermo-kinetic multi-zone modelling of low temperature combustion engines, Prog. Energy Combust. Sci. 91 (2022) 100998, https://doi.org/10.1016/j.pecs.2022.100998.